Small-x phenomenology – summary and status 2002

The Small-x Collaboration

J.R. Andersen[1], S. Baranov[2], J. Collins[3], Y. Dokshitzer[4], L. Goerlich[5], G. Grindhammer[6], G. Gustafson[7], L. Jönsson[8], H. Jung[8], J. Kwieciński[5,†], E. Levin[9], A. Lipatov[10], L. Lönnblad[7], M. Lublinsky[9], M. Maul[7], I. Milcewicz[5], G. Miu[7], G. Nowak[5], T. Sjöstrand[7], A. Staśto[11], N. Tîmneanu[12], J. Turnau[5], N. Zotov[13]

[1] DAMTP and Cavendish Laboratory, University of Cambridge, UK
[2] Lebedev Institute of Physics, Moscow, Russia
[3] Penn State Univ., 104 Davey Lab., University Park PA 16802, USA
[4] LPTHE, Universités P. & M. Curie (Paris VI) et Denis Diderot (Paris VII), Paris, France
[5] H. Niewodniczanski Institute of Nuclear Physics, Cracow, Poland
[6] Max Planck Institut, Munich, Germany
[7] Department of Theoretical Physics, Lund University, Sweden
[8] Department of Physics, Lund University, Sweden
[9] School of Physics, Tel Aviv University, Tel Aviv, Israel
[10] Moscow State University, Moscow, Russia
[11] DESY, Hamburg, Germany and H. Niewodniczanski Institute of Nuclear Physics, Cracow, Poland
[12] University of Uppsala, Sweden
[13] Skobeltsyn Institute of Nuclear Physics, Moscow State University, Moscow, Russia
[†] deceased

This paper is dedicated to the memory of Jan Kwieciński, who died unexpectedly on August 29, 2003.

Abstract. A second workshop on small-x physics, within the Small-x Collaboration, was held in Lund in June 2002 with the aim of over-viewing recent theoretical progress in this area and summarizing the experimental status.

1 Introduction

This paper is a summary of the 2nd workshop on small-x parton dynamics held in Lund in the beginning of June 2002. During two days we went through a number of theoretical, phenomenological as well as experimental aspects of small-x physics in short talks and long discussions. Whereas our first workshop in 2001 and the resulting summary paper [1] was dedicated to a general survey and discussion of small-x physics in order to identify the most pending questions, we concentrate here on those aspects, where progress has been made, as well as on a more detailed discussion and some aspects of the experimental situation. For a general introduction to small-x physics and the small-x evolution equations, as well as tools for calculation in terms of Monte Carlo programs, we refer the reader to [1].

With the successful completion of the two full hadron level Monte Carlo programs LDCMC [2–5] and Cascade [6, 7], the necessary tools were provided for detailed studies both on a theoretical and phenomenological level as well as for detailed comparison with experimental data and the usage in the experimental groups at HERA and else-

where. Since then they have been used in very different areas, like jet production and heavy flavor physics. The small-x improved unintegrated parton densities obtained from CCFM evolution implemented in the Monte Carlo generators have been proven to be a very powerful tool in describing experimental data as well as for estimating the effect of higher order corrections. For example only by also applying the Cascade Monte Carlo in the extraction of F_2^c and in the calculation of bottom production at HERA, it was recognized that the extrapolation from the measured visible range to the total cross section is dangerous and introduces large model dependencies. Now, in the area of bottom production, the visible cross sections are in reasonable agreement both with calculations applying $k_\perp$-factorization with CCFM evolved unintegrated gluon density as well as with NLO calculations in the collinear approach. This shows the importance of applying alternative approaches even when extracting experimental measurements.

This paper is organized as follows: First we discuss in more detail the definition of unintegrated gluon densities, as well as the question of gauge invariance of parton densities

in general and especially of the $k_\perp$-factorization approach. In the following section we discuss results and problems in theoretical applications of the unintegrated parton distribution functions, different parameterizations, the scale in α_s, the role of the non-singular terms in the $g \to gg$ splitting function, saturation and the effects of energy momentum conservation in the BFKL equation. The section also contains a discussion of polarized unintegrated distributions, polarization effects and color octet contributions in J/ψ meson production. The second part of this paper deals with experimental investigations of small-x effects and with the question, whether and where deviations from the collinear approach can be established, and whether a sign for a new evolution scheme like BFKL/ CCFM/ LDC has already been seen. We end this paper with an outlook and a definition of the next steps and goals.

2 $k_\perp$-factorization formalism

The DGLAP [8–11] evolution treats successive parton emissions which are strongly ordered in virtuality and resums the resulting large logarithms of ratios of subsequent virtualities. Because of the strong ordering of virtualities, the virtuality of the parton entering the hard scattering matrix element can be neglected (treated collinear with the incoming hadron) compared to the large scale Q^2.

At very high energies, it is believed that the theoretically correct description is given by the BFKL [12–14] evolution. Here, each emitted gluon is assumed to take a large fraction, $1 - z|_{z\to 0}$ of the energy of the propagating gluon, and large logarithms of $1/z$ are summed up to all orders.

The CCFM [15–18] evolution equation resums also large logarithms of $1/(1-z)$ in addition to the $1/z$ ones. Furthermore it introduces angular ordering of emissions to correctly treat gluon coherence effects. In the limit of asymptotic energies, it is almost equivalent to BFKL [19–21], but also similar to the DGLAP evolution for large x and high Q^2. The cross section is $k_\perp$-factorized into an off-shell matrix element convoluted with an unintegrated parton density (uPDF), which now also contains a dependence on the maximum angle Ξ allowed in emissions. This maximum allowed angle Ξ is defined by the hard scattering quark box, producing the (heavy) quark pair and also defines the scale for which parton emissions are factorized into the uPDF.

The original CCFM splitting function is given by

$$\tilde{P}_g(z_i, \bar{q}_i^2, {k_{\perp i}}^2) \tag{1}$$
$$= \frac{\bar{\alpha}_s(\bar{q}_i^2(1-z_i)^2)}{1-z_i} + \frac{\bar{\alpha}_s({k_{\perp i}}^2)}{z_i}\Delta_{\text{ns}}(z_i, \bar{q}_i^2, {k_{\perp i}}^2),$$

with $\bar{\alpha}_s = \frac{3\alpha_s}{\pi}$ and the non-Sudakov form factor Δ_{ns} given by

$$\ln\Delta_{\text{ns}}(z_i, \bar{q}_i^2, {k_{\perp i}}^2)$$
$$= -\int_{z_i}^1 \frac{\mathrm{d}z'}{z'}\int\frac{\mathrm{d}q^2}{q^2}\bar{\alpha}_s\cdot\Theta(k_{\perp i}-q)\Theta(q-z'\bar{q}_i) \tag{2}$$

$$= -\int_{z_i}^1\frac{\mathrm{d}z'}{z'}\int_{(z'\bar{q}_i)^2}^{{k_{\perp i}}^2}\frac{\mathrm{d}q^2}{q^2}\bar{\alpha}_s. \tag{3}$$

The angular ordering condition is given by

$$z_{i-1}\bar{q}_{i-1} < \bar{q}_i, \tag{4}$$

where the rescaled transverse momenta $\bar{q}_i$ of the emitted gluons is defined by

$$\bar{q}_i = \frac{p_{\perp i}}{1-z_i}. \tag{5}$$

Here $z_i = x_i/x_{i-1}$ is the ratio of the energy fractions in the branching $(i-1) \to i$ and $p_{\perp i}$ is the transverse momentum of the emitted gluon i. The transverse momentum of the propagating gluon is given by $k_{\perp i}$. It is interesting to note, that the angular ordering constraint, as given by (4), reduces to ordering in transverse momenta $p_\perp$ for large z, whereas for $z \to 0$, the transverse momenta are free to perform a so-called random walk.

In [1] it has been proposed to include also the non-singular terms in the splitting function as well as to consistently use $\mu_r = p_\perp$ for the renormalization scale in $\alpha_s(\mu_r)$, everywhere. These changes, although formally sub-leading, have significant influence for calculations performed at present collider energies.

The inclusion of non-singular terms, as well as the evolution of quarks, is straightforward in the LDC model [2–5], which is a reformulation of CCFM, where the separation between the initial- and final-state emissions is redefined. In addition to the angular ordering in (4), the gluons emitted in the initial state are required to have

$$p_{\perp i} > \min(k_{\perp i}, k_{\perp i-1}). \tag{6}$$

In the double leading-logarithmic approximation (DLLA), this requires a reweighting of each splitting, completely canceling the non-Sudakov form factor, reducing the splitting function in (1) to the leading singularities of the standard DGLAP one, making the inclusion of non-singular terms as well as quark splittings a trivial exercise. The constraint in (6) means that the $p_\perp$ of the emitted gluon is always close to the highest scale in the splitting and the argument in α_s is naturally taken to be $p_\perp^2$.

While formally equivalent to the DLLA accuracy for the inclusive observable F_2, it is important to note that the sets of chains of initial-state splittings summed over, are different in LDC and CCFM. Therefore results for exclusive final states agree only after addition of final-state radiation in the appropriate kinematical regions (which are different in the two formalisms).

We here also want to mention the formalisms developed in [22, 23]. An evolution equation for a single scale uPDF, which interpolates between DGLAP and BFKL, is presented by Kwieciński, Martin and Staśto in [22]. The formalism for a two-scale uPDF by Kimber, Martin and Ryskin [23] is based on the same single scale evolution equation, but an angular cut is applied for the last step in the chain.

2.1 Unintegrated parton distributions

In the following we discuss in detail the precise definition of (integrated or unintegrated) parton density functions (PDFs) [24].

(1) A PDF is not a physical quantity in and of itself. It merely is a useful tool.

(2) A PDF is often given as a probability density of quarks or gluons within the framework of light-front quantization of QCD in the light-cone gauge. Such a definition is useful to provide motivation, intuition and an initial candidate for a formal definition. But this method does not necessarily provide a valid definition.

(3) Whether or not some kind of consistent probability interpretation can be made with modified definitions is an open question. For many applications of PDFs, the answer to this question is irrelevant.

(4) The physical significance of PDFs is that there are factorization formulae involving them[1]. Factorization formulae (in their most general sense) give approximations to physical amplitudes or cross sections that are useful and predictive because:

(a) the PDFs are universal – the same in a range of different processes and situations;

(b) some (not necessarily all) of the coefficients in a factorization formula may be estimated, for example in fixed-order perturbation theory with a weak coupling;

(c) kernels of evolution equations (DGLAP etc.) may similarly be estimated perturbatively.

(5) Since a PDF will include non-perturbative physics, it is generally desirable that an explicit definition be given, for example in terms of some Green function or a matrix element of some (usually non-local) operator.

(6) Given point (1), it is not necessary that a PDF's definition is explicitly gauge invariant. However, if the definition is not gauge invariant, the choice of gauge must be explicitly specified. It should be possible to transform the PDF's definition into an explicitly gauge-invariant form. But in general there should be (an) extra parameter(s) for the parton density corresponding perhaps to a gauge-fixing vector or the direction of Wilson line factors in the operators. It will also be necessary to obtain evolution equations with respect to the extra variable(s). See the work of Dokshitzer, Diakonov and Troian [25] and of Collins and Soper [26, 27] for example.

(7) The most obvious candidate definition for a PDF is as a number density in the light-cone gauge, essentially

$$f(x, k_\perp) = \frac{\langle p|b_k^\dagger b_k|p\rangle}{\langle p|p\rangle}, \tag{7}$$

where $b_k^\dagger$ and b_k are creation and annihilation operators for a flavor of parton in the sense of light-front quantization in light-cone gauge. However, as we will see below, such a definition is divergent beyond the lowest order of perturbation theory.
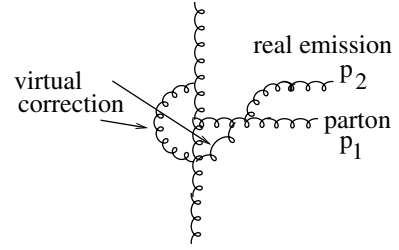

Fig. 1. A schematic drawing indicating the real and virtual corrections in a parton splitting process. The transverse momentum of the emitted parton p_2 is limited by the emitting parton p_1, whereas the transverse momenta in the virtual loops can reach any value

(8) The divergence arises from an integral over rapidity of emitted gluons and is present even if all IR and UV divergences are regulated. The divergence is an endpoint divergence due to the $1/k^+$ singularity in the gluon propagator in light-cone gauge: $\int_0 dk_+/k_+$. Therefore it cannot be removed by a modification of the integration path, and in that way changing the analytic prescription of the singularity.

(9) For an uPDF, the divergence cannot be canceled between real final-state and virtual gluon emission: Virtual gluon emission has an unrestricted transverse momentum integral, but real gluon emission is restricted by the transverse momentum of the emitting parton (Fig. 1). Hence a cancellation of real and virtual divergences cannot occur simultaneously for all values of the transverse momentum of the emitted parton. This is a problem because without a cancellation between real and virtual divergencies the resulting parton density function diverges and becomes meaningless.

(10) The rapidity divergence ($\int dk_+/k_+ = \int_{-\infty} dy$) involves gluon momenta in a region that has no relevance to the process: The momenta have infinite rapidity relative to physical particles. Any sensible definition of a PDF must have a cutoff. A simple candidate would be obtained by taking the (incorrect) light-cone gauge definition but with the use of a planar gauge: $n \cdot A = 0$, with $n^2 \neq 0$. The unintegrated parton density then has *two* extra parameters beyond the x and $k_\perp$ kinematic variables. These are the inevitable renormalization scale μ and the variable $(p \cdot n)^2/n^2 p^2$. The renormalization scale μ has the approximate interpretation of a cutoff on the transverse momentum or the virtuality of virtual particles, and the last variable equals $\cosh^2 y$, where y is the rapidity difference between the target and the gauge-fixing vector.

(11) In the CCFM formalism these two extra parameters are correlated. Thus the CCFM parameter $\bar{q}$ determines both the transverse momentum cutoff and the limiting rapidity in the p-rest frame through the relation $y = \ln(\bar{q}/m_p x_g)$.

(12) In [24] Collins has proposed explicit gauge-invariant definitions of unintegrated PDFs that avoid the difficulties mentioned above. The evolution equation would be the one given by Collins, Soper and Sterman [26, 27]. Details in this approach are being worked out.

---

[1] The status of a given factorization formula may be anywhere from being a completely proved theorem to merely being a conjecture.

2.2 Further questions on gauge invariance

The question of gauge invariance[2] is not only relevant in the discussion of PDFs, but also for $k_\perp$-factorization in general as well as for the cross sections which are $k_\perp$-factorized [28–31] into an off-shell ($k_\perp$-dependent) partonic cross section $\hat{\sigma}\left(\frac{x}{z}, k_\perp{}^2\right)$ and a $k_\perp$-unintegrated parton density function[3] $\mathcal{F}(z, k_\perp{}^2)$:

$$\sigma = \int \frac{\mathrm{d}z}{z} \mathrm{d}^2 k_\perp \hat{\sigma}\left(\frac{x}{z}, k_\perp{}^2\right) \mathcal{F}\left(z, k_\perp{}^2\right). \qquad (8)$$

Here the partons generating a QCD hard process are off-mass shell. On-shell amplitudes in, say, dimensional regularization are supposed to be gauge invariant, if not yet physical. The ensuing factorization of mass singularities, introduces a scheme and perhaps a gauge dependence, to be canceled by (integrated) PDFs in a physical process involving hadrons. Thus, any gauge dependence introduced in the PDFs is in a sense an artifact of the factorization procedure.

A single off-shell gluon is not gauge invariant. However, experience with string theory [32] suggests that high-energy factorization could be a way of defining a physical off-shell continuation, as residue of the Regge pole exchanged at the given (off-shell) momentum transfer. In such a case the $k_\perp$ cannot be assigned to a single gluon (except in some approximation) because the Reggeon is a compound state of (infinitely) many partons. Therefore, implementing such an idea in a formal definition is hard and further complicated by the fact that gluon Reggeization is infrared singular.

The work on $k_\perp$-factorization by [30] provided a gauge-invariant definition of off-shell matrix elements, based on the Regge-gluon factorization idea.[4] The gluon Green function (and related uPDF) was defined so as to satisfy the (gauge-independent) BFKL equation, and the emphasis was on defining the corresponding off-shell matrix elements, given the physical cross section.

At leading-log level, CCH [30] noticed that the LO off-shell matrix elements could be defined by the high-energy limit of an on-shell six-point function (or an eight-point function in the two-$k_\perp$ case) whose expression was worked out in a physical gauge first, and then translated to the Feynman gauge. Because of their definition, the LO matrix elements are gauge invariant and positive definite. At next-to-leading parton level Ciafaloni [33], and Ciafaloni and Colferai [34] noticed that one has to subtract, however, the leading kernel contribution (including gluon Reggeization) in order to avoid a rapidity divergence related to the $\ln(s)$

term in the total cross section. This subtraction introduces a factorization-scheme dependence, mostly on the choice of the scale of the process, but not a gauge dependence. Recently the DESY group [35–37] went a long way towards completing this approach for DIS and jet production. The NLO matrix elements so defined are gauge invariant, while positivity has not yet been thoroughly investigated, and is not guaranteed, because of the subtraction. The latter is devised so as to put the whole energy dependence in the Green function.

The CCFM equation employs a definition of unintegrated density as a sum over physical final states, restricted to some angular region via angular ordering. This definition with rapidity cutoff is consistent with the subsequent analysis of matrix elements because the latter roughly provide upper and lower bounds on the rapidity integration, due to the angular coherence property. However, the relation of CCFM to BFKL was worked out at leading log (LL) only, and no complete attempt has been made so far to match this definition to exact next-to-leading log (NLL) calculations. In this case the energy dependence of the physical cross section is shared between density and matrix elements, depending on the choice of the cutoff.

The conclusion of the above considerations is that any prediction for a physical process must be, obviously, gauge invariant, however (unintegrated) PDF's are not guaranteed to be so. The formulation of $k_\perp$-factorization was meant to be gauge invariant, and has been carried through at LL by [30, 31] and at NLL level by [34, 38, 39]. It is not yet clear whether gauge invariance is restored beyond that level. However, gauge-dependent definitions of PDF's with the corresponding matrix elements can be conceived also, provided their convolution reproduces the same (physical) cross section.

3 Theoretical applications

3.1 Comparison of available parameterizations

The original CCFM splitting function given in (1) includes only the singular terms as well as a simplified treatment of the scale in α_s, i.e. $k_\perp$ was used as the scale in the $1/z$ term and the non-Sudakov factor whereas $p_\perp$ was used in the $1/(1-z)$ term and in the Sudakov form factor. Due to the angular ordering a kind of random walk in the propagator gluon $k_\perp$ can be performed, and therefore care has to be taken for small values of $k_\perp$. Even during the evolution the non-perturbative region can be entered for $k_\perp < k_\perp{}^\mathrm{cut}$. In the region of small $k_\perp$, α_s and the parton density are large, and collective phenomena, like gluon recombination or saturation might play a role. Thus, the fast increase of the parton density and the cross section is tamed. However, for the calculation of the unintegrated gluon density presented here, a simplified but practical approach is taken: no emissions are allowed for $k_\perp < k_\perp{}^\mathrm{cut}$ and $q_\perp < Q_0$. The limitation of $k_\perp$ is necessary for the calculation of the non-Sudakov form factor Δ_ns in (3) and it ensures a finite value of $\alpha_\mathrm{s}(k_\perp)$. Different choices of $k_\perp{}^\mathrm{cut}$ are discussed below.

---

[2] This section is based on some remarks by M. Ciafaloni (unpublished) during a discussion with John Collins and Yuri Dokshitzer.

[3] We use the classification scheme introduced in [1]: $x\mathcal{G}(x, k_\perp{}^2)$ describes DGLAP type unintegrated gluon distributions, $x\mathcal{F}(x, k_\perp{}^2)$ is used for pure BFKL and $x\mathcal{A}(x, k_\perp{}^2, \bar{q}^2)$ stands for a CCFM type or any other type involving two scales.

[4] Note that there are certain issues on gauge invariance which the authors of [24,30] have not been able to resolve completely, but which will be a topic of future work.

Following the arguments in [1], the scale in α_s was changed to $p_\perp = q(1-z)$ everywhere, and the CCFM splitting function was extended to include also the non-singular terms [40,41]. The unintegrated gluon density at any x, $k_\perp$ and scale $\bar{q}$ is obtained by evolving numerically [6] a starting gluon distribution from the scale Q_0 according to CCFM to the scale $\bar{q}$. The normalization N of the input distribution as well as the starting scale Q_0, which also acts as a collinear cutoff to define $z_{\max} = 1 - Q_0/q$, need to be specified. These parameters were fitted such that the structure function F_2 as measured at H1 [42,43] and ZEUS [44,45] can be described after convolution with the off-shell matrix element in the region of $x < 5 \cdot 10^{-3}$ and $Q^2 > 4.5\,\mathrm{GeV}^2$. Using 248 data points a $\chi^2/\mathrm{ndf} = 4.8, 1.29, 1.18, 1.83$ for **JS, J2003 set 1,2,3**, respectively, is obtained. The following sets of CCFM unintegrated gluon densities are obtained.

(1) **JS** (Jung, Salam [6]). The splitting function P_{gg} of (1) is used. The soft region is defined by $k_\perp^{\mathrm{cut}} = 0.25\,\mathrm{GeV}$.

(2) **J2003 set 1** (Jung [41]). The splitting function P_{gg} of (1) is used, with $k_\perp^{\mathrm{cut}} = Q_0$ fitted to $k_\perp^{\mathrm{cut}} = Q_0 = 1.33\,\mathrm{GeV}$.

(3) **J2003 set 2**. The CCFM splitting function containing also the non-singular terms is used:

$$P(z, q, k)$$
$$= \bar{\alpha}_s\left(k_\perp^{\,2}\right) \cdot \left(\frac{(1-z)}{z} + z(1-z)/2\right) \Delta_{\mathrm{ns}}(z, q, k)$$
$$+ \bar{\alpha}_s\left((1-z)^2 q^2\right)\left(\frac{z}{1-z} + z(1-z)/2\right). \qquad (9)$$

The Sudakov and non-Sudakov form factors were changed accordingly. The collinear cut is fitted to $Q_0 = k_\perp^{\mathrm{cut}} = 1.18\,\mathrm{GeV}$.

(4) **J2003 set 3**. The CCFM splitting function contains only singular terms, but the scale in α_s is changed from $k_\perp$ to $p_\perp$ for the $1/z$ term. The collinear cut is fitted to $Q_0 = k_\perp^{\mathrm{cut}} = 1.35\,\mathrm{GeV}$. The problematic region in the non-Sudakov form factor in (3) is avoided by fixing $\alpha_s(\mu_r)$ for $\mu_r < 0.9\,\mathrm{GeV}$.

A comparison of the different sets of CCFM unintegrated gluon densities is shown in Fig. 2. It is clearly seen that the treatment of the soft region, defined by $k_\perp < k_\perp^{\mathrm{cut}}$ influences the behavior at small x and small $k_\perp$.

Also the LDC model describes F_2 satisfactorily, but the corresponding unintegrated gluon densities are somewhat different. One major difference as compared to CCFM is that LDC can also include quarks in the evolution and can therefore also reproduce F_2 in the valence region of high x. In Fig. 3 three different unintegrated gluon densities for the LDC approach are presented. The *standard* set refers to the full LDC including quarks in the evolution and the full gluon splitting function, whereas for the *gluonic* set and the *leading* set only gluon evolution is considered with only singular terms in the splitting function for the latter. All three alternatives have been individually fitted to F_2 in the region $x < 0.3$, $Q^2 > 1.5\,\mathrm{GeV}^2$ for *standard* and $x < 0.013$ and $Q^2 > 3.5\,\mathrm{GeV}^2$ for *gluonic* and *leading*. In LDC there is only one relevant infrared cutoff, $k_{\perp 0}$, which limits the $p_\perp$ of the emitted gluons. This has been fitted
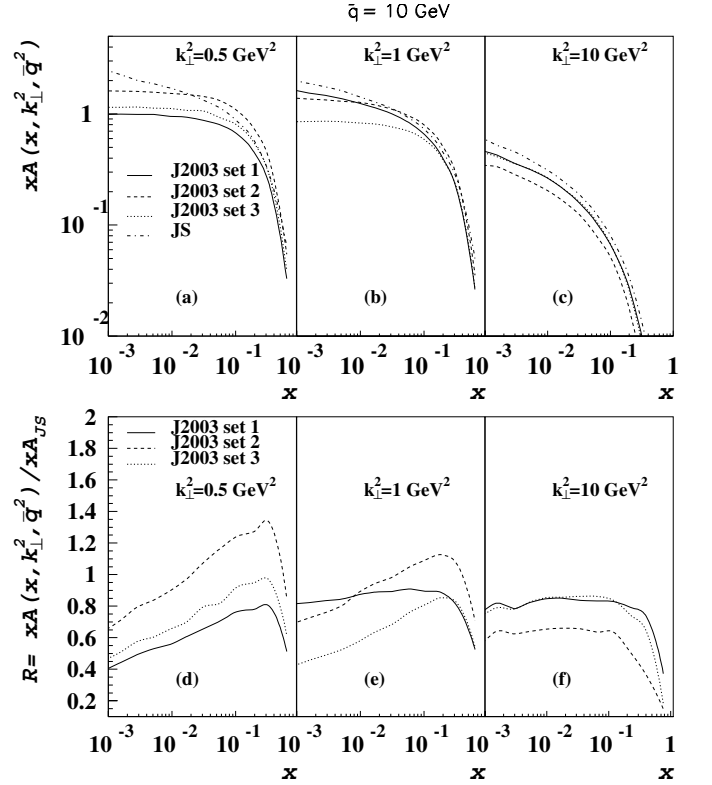

Fig. 2. Comparison of the different sets of unintegrated gluon densities obtained from the CCFM evolution as described in the text. In (a)–(c) the unintegrated gluon density is shown as a function of x for different values of $k_\perp$ at a scale of $\bar{q} = 10\,\mathrm{GeV}$. In (d)–(f) the ratio $R = \frac{x\mathcal{A}(x, k_\perp^{\,2}, \bar{q}^2)}{x\mathcal{A}(x, k_\perp^{\,2}, \bar{q}^2)_{\mathrm{JS}}}$ as a function of x for different values of $k_\perp$ is shown
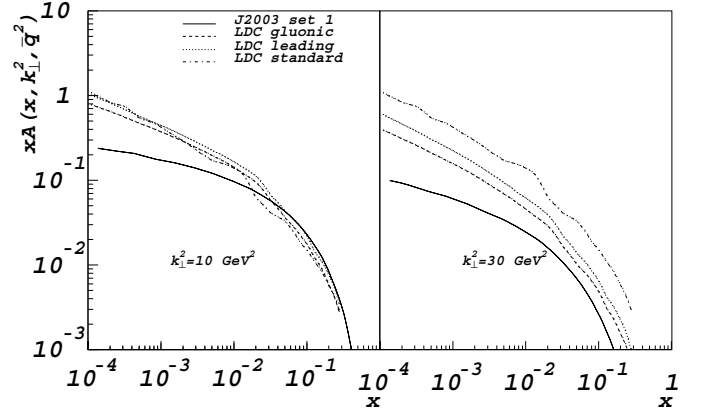

Fig. 3. Comparison of the different sets of unintegrated gluon densities obtained within LDC at scale of $\bar{q} = 10\,\mathrm{GeV}$. *Standard* refers to the full LDC including quarks in the evolution and the full gluon splitting function. For *gluonic* and *leading* only gluon evolution is considered with only singular terms in the splitting function for the latter. Also shown is the J2003 set 1 for comparison (divided by π)

to 0.99, 1.80 and 1.95 for *standard*, *gluonic* and *leading* respectively. No cut on the transverse momenta of the virtual gluons is applied and the argument μ_r in α_s is set to $\mu_r = p_\perp$ which is then always larger than the cutoff $k_{\perp 0}$.

3.2 Semi-analytical insight into the CCFM equation

The CCFM equation interlocks in a rather complicated way the two relevant scales, i.e. the transverse momentum $k_\perp$ of the parton and the hard scale $\bar{q}$ which is related to the maximal emission angle. Due to this complexity the existing analyses of the CCFM equation are based upon numerical solutions. After performing some approximations it is however possible to obtain semi-analytical insight into the CCFM equation and we would like to consider the following two cases:
(1) the single loop approximation (SLA) [46–48], which corresponds to the DGLAP limit;
(2) the CCFM equation at small x with consistency constraint (CC) [3, 49].

3.2.1 The single loop approximation

This approximation corresponds to setting the non-Sudakov form factor equal to unity and to the replacement of the angular ordering by a $q_\perp$ ordering. It can be a reasonable approximation for large and moderately small values of x. In Fig. 4 we show a comparison of the unintegrated gluon density obtained in the full CCFM and the single loop approximation (using the same input distributions). In SLA the CCFM equation can be partially diagonalized by the Fourier–Bessel transform of the unintegrated gluon distribution $\mathcal{A}(x, k_\perp, \bar{q})$ [50]

$$\mathcal{A}(x, k_\perp, \bar{q}) = \int_0^\infty db\, b J_0(k_\perp, b) \bar{\mathcal{A}}(x, b, \bar{q}), \qquad (10)$$

$$\bar{\mathcal{A}}(x, b, \bar{q}) = \int_0^\infty dk_\perp\, k_\perp J_0(k_\perp, b) \mathcal{A}(x, k_\perp, \bar{q}), \quad (11)$$

with b being the impact parameter and the integrated gluon distribution is given by

$$xg(x, Q^2) = 2\bar{\mathcal{A}}\left(x, b = 0, \bar{q} = \sqrt{Q^2}\right). \qquad (12)$$

The transverse coordinate representation also partially diagonalizes the CCFM equation extended for polarized unintegrated par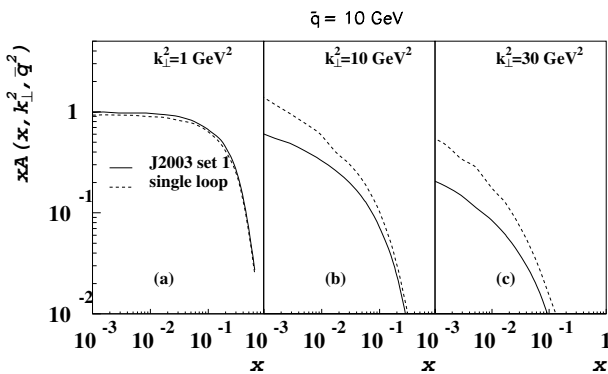ton distributions as will be discussed in a separate section below. Due to the absence of the $1/z$ term in the polarized splitting function it will be possible to utilize this representation *beyond* the single loop case (see Sect. 2.6). The tranverse coordinate representation has also been used for the analysis of the CCFM equation in SLA for the unintegrated gluon distributions in a photon [51].

The CCFM equation in SLA takes the following form in the b representation:

$$\bar{\mathcal{A}}(x, b, \bar{q}) = \bar{\mathcal{A}}^0(x, b)$$
$$+ \int_{q_0^2}^{\bar{q}^2} \frac{dq^2}{q^2} \frac{\alpha_s(q^2)}{2\pi} \int_0^1 \frac{dz}{z} z P_{gg}(z)$$
$$\times \left\{ \Theta(z - x) J_0[b(1-z)q] \bar{\mathcal{A}}\left(\frac{x}{z}, b, q\right) \right.$$
$$\left. - z \bar{\mathcal{A}}(x, b, q) \right\}, \qquad (13)$$

where for simplicity we have neglected the quark contribution. At $b = 0$ this equation reduces to the conventional DGLAP evolution equation in the integral form. Equation (13) can be solved in a closed form using the moment function

$$\bar{f}_\omega(b, \bar{q}) = \int_0^1 dx\, x^{\omega-1} \bar{\mathcal{A}}(x, b, \bar{q}). \qquad (14)$$

Different approximations of (13) are related to formalisms used e.g. in studies of Drell–Yan pairs and can give more insight into the properties of the solutions to the CCFM equation. Thus approximations in the Bessel function and the Sudakov form factor gives the relation [50]

$$\mathcal{A}(x, k_\perp, \bar{q}) \simeq \frac{T_g(b = 1/k_\perp, \bar{q})}{k_\perp^2} \qquad (15)$$
$$\times \int_0^{1 - k_\perp/\bar{q}} dz P_{gg}(z) \cdot \frac{\alpha_s(k_\perp^2)}{2\pi} \Theta(z - x) \frac{x}{z} g\left(\frac{x}{z}, k_\perp^2\right),$$

where the Sudakov form factor $T_g(b, \bar{q})$ is defined by

$$T_g(b, \bar{q}) = \exp\left[-\int_{1/b^2}^{\bar{q}^2} \frac{dq^2}{q^2} \frac{\alpha_s(q^2)}{2\pi} \int_0^{1 - 1/(bq)} dz\, z P_{gg}(z) \right]. \qquad (16)$$

Neglecting also contributions to the Sudakov form factor for large q^2 gives

$$\mathcal{A}(x, k_\perp, \bar{q}) \simeq \frac{\partial [T_g(b = 1/k_\perp, \bar{q}) xg(x, k_\perp^2)]}{\partial k_\perp^2}. \qquad (17)$$

The approximate expressions (17) and (15) are similar to those discussed in [23, 25, 52]. It turns out that expression (15) gives a reasonable approximation of the exact solution of the CCFM equation in SLA while expression (17) can generate negative result for large $k_\perp$ and large $x \sim 0.1$ [50].

3.2.2 CCFM equation with consistency constraint

We shall consider now the CCFM equation in the small-x limit keeping only the singular $1/z$ part of the splitting

Fig. 4. Comparison of the unintegrated gluon densities obtained in the CCFM and single loop approximation, using the same input distributions of J2003 set 1

function $P_{gg}(z)$ and neglecting the Sudakov form factor. We shall also impose the consistency constraint [3,49] which is known to generate the dominant part of the sub-leading BFKL corrections. The integration limit(s) in the CCFM equation are now constrained by the following competing conditions:[5]

(1) angular ordering (AO) $\leftrightarrow z_{i-1}\bar{q}_{i-1} < \bar{q}_i$;

(2) consistency constraint (CC) $\leftrightarrow \bar{q}_i^2 < k_{\perp}^2/z_i$.

It can easily be observed that CC takes over AO for $k_{\perp}^2 < \bar{q}^2/z$.

The structure of the CCFM equation at small x with CC is different in the regions $k_\perp < \bar{q}$ and $k_\perp > \bar{q}$. At $k_\perp < \bar{q}$ the unintegrated distribution $\mathcal{A}(x, k_\perp, \bar{q})$ is independent of $\bar{q}$, i.e.,

$$\mathcal{A}(x, k_\perp, \bar{q}) \to \mathcal{F}(x, k_\perp), \tag{18}$$

after adopting the leading $\ln^2(k_{\perp}^2/\bar{q}^2)$ approximation of the Sudakov form factor, while for $k_\perp > \bar{q}$ we get the following expression after adopting the leading double $\ln^2(k_{\perp}^2/\bar{q}^2)$ approximation:[6]

$$\mathcal{A}(x, k_\perp, \bar{q}) = \mathcal{F}(x, k_\perp) \exp\left[-\frac{3\alpha_{\rm s}}{2\pi} \ln^2(k_{\perp}^2/\bar{q}^2) \right], \tag{19}$$

where for simplicity we keep fixed $\alpha_{\rm s}$. The single scale function $\mathcal{F}(x, k_\perp)$ satisfies the BFKL-like equation with sub-leading corrections. We found in this way that imposing the consistency constraint and the double $\ln^2(k_{\perp}^2/\bar{q}^2)$ approximation in the region $k_\perp > \bar{q}$ we reduce the two-scale problem to the single scale one and to the BFKL-like dynamics. The novel feature of the CCFM framework is however the exponential suppression of the unintegrated distribution in the region $k_\perp \gg \bar{q}$ (cf. (19)) due to the double $\ln^2(k_{\perp}^2/\bar{q}^2)$ effects [15]. They are of course formally sub-leading at small x.

3.3 Effects of phase space constraints in BFKL

The leading-logarithmic (LL) BFKL formalism resums terms in the perturbative series of the form $(\alpha_{\rm s} \ln(\hat{s}/s_0))^n$, where $\hat{s}$ is the square of the center of mass energy for the hard scattering and s_0 some perturbative scale separating the evolution of the t-channel exchange from the matrix elements. These logarithms arise due to the emission of gluons from the t-channel exchange. For the scattering of two particles $p_A p_B \to k_a k_b k_i$ where k_i are the momenta of the gluons emitted from the BFKL evolution, we have $\hat{s} = 2p_A p_B$ and s_0 is often chosen as $s_0 = k_{a\perp}k_{b\perp}$ with $k_{a\perp}$ ($k_{b\perp}$) the transverse part of k_a (k_b respectively). In deep inelastic scattering large $\hat{s}$ corresponds to small x of the probed parton. For hadronic dijet production, large $\hat{s}$ corresponds to large separation in rapidity between the leading jets, and therefore to moderate values of x, where normal

DGLAP evolution of the partons is valid (and therefore the standard PDFs can be used [53]). The next-to-leading logarithmic corrections [33, 54] consist of terms proportional to $\alpha_{\rm s}(\alpha_{\rm s} \ln(\hat{s}/s_0))^n$, i.e. suppressed by one power of $\alpha_{\rm s}$ compared to the LL component. The logarithms resummed in the BFKL approach correspond to the enhanced terms in scattering processes for large center of mass energies and also the enhanced terms in the description of the small-x behavior of the gluon distribution function.

When confronting BFKL predictions with data, several points are worth observing. First of all, present day colliders do not operate at "asymptotic energies" where the high-energy exponent dominates the BFKL prediction under the assumption that the coupling can be held fixed and small, leading to a prediction of an exponential rise in cross section with an intercept of $\bar{\alpha}_{\rm s} 4 \ln 2$, with $\bar{\alpha}_{\rm s} = \frac{3\alpha_{\rm s}}{\pi}$. For example at HERA, the separation between the struck quark and the forward jet can reach up to about four units of rapidity, whereas the measurable jet separation at the Tevatron is up to six units. This is not asymptotically large. Secondly, it should be remembered that the logarithms resummed are kinematically generated, and in the derivation of the standard analytic solution to the BFKL equation, the transverse momentum of the gluons emitted from the BFKL evolution has been integrated to infinity. It is therefore apparent that any limits on the phase space probed in an experiment can have a crucial impact on the theoretical prediction. Such limits can either be the cuts implemented in the measurement or the limits on the available energy at a collider. The total available energy will affect the impact factors, while taking into account also detailed energy-momentum conservation in each gluon emission will in addition affect the BFKL exponent. Taking hadronic dijet production as an example, the energy constraint will obviously not just limit the possible rapidity separation of the leading dijets, but also the amount of possible radiation from the BFKL evolution, especially when the leading dijets are close to the kinematical boundary. For a multi-particle final state described by two leading dijets with transverse momentum and rapidity $(p_{a/b\perp}, y_{a/b})$ and n gluons described by $(k_{\perp i}, y_i)$, the total energy of the event is given by $\hat{s} = x_a x_b s$ where s is the square of the total energy of the hadron collider and

$$x_a = \frac{p_{a\perp}}{\sqrt{s}}{\rm e}^{y_a} + \sum_{i=1}^{n} \frac{k_{i\perp}}{\sqrt{s}}{\rm e}^{y_i} + \frac{p_{b\perp}}{\sqrt{s}}{\rm e}^{y_b},$$

$$x_b = \frac{p_{a\perp}}{\sqrt{s}}{\rm e}^{-y_a} + \sum_{i=1}^{n} \frac{k_{\perp i}}{\sqrt{s}}{\rm e}^{-y_i} + \frac{p_{b\perp}}{\sqrt{s}}{\rm e}^{-y_b}. \tag{20}$$

While it can be argued that the contribution to $\hat{s}$ from the gluons emitted from the BFKL evolution is sub-leading compared to the contribution from the leading dijets, it is not obvious that the effect on the cross section is small, simply for the reasons mentioned above: ignoring the contribution to the parton momentum fractions will resum logarithmically enhanced contributions from regions of phase space that lie outside what can be probed at a given collider. Here we have taken as an example dijet production at a hadron collider, but a similar effect will be found for

---

[5] The single loop approximation is extended, since the $\bar{q}$ ordering is replaced by angular ordering

[6] Double $\ln(k_t^2/\bar{q}^2)$ terms appear in the Sudakov form factor for exclusive cross sections. They are not present in the inclusive cross section, which is $\propto F_2$
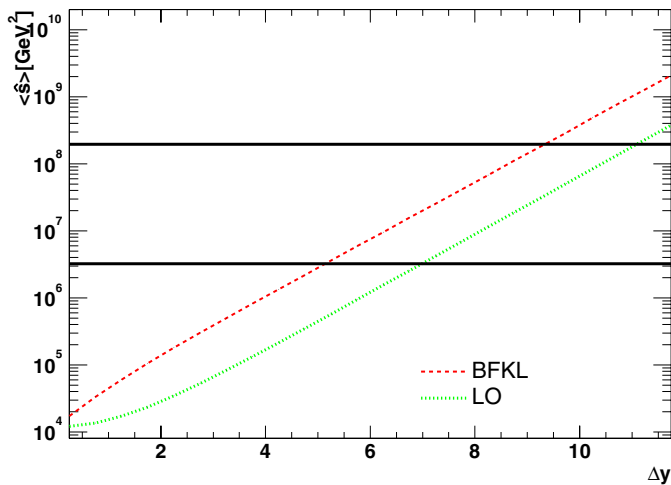
Fig. 5. The average center of mass energy in $gg \to gg$ scattering with (red/dashed) and without (green/dotted) BFKL evolution of the t-channel gluon, with $p_{\perp\min} = 20\,\mathrm{GeV}$ for the dijets and $\alpha_s = 0.1635$. Also plotted is the hadronic center of mass energy squared for the Tevatron $((1.8\,\mathrm{TeV})^2)$ and the LHC$((14\,\mathrm{TeV})^2)$

Fig. 6. The 0–, 1, 2–, 3– and 4–jet parton level cross sections as a function of the cutoff μ_R, for a rapidity span of $\Delta y = 5$ and $p_{\perp\min} = 20\,\mathrm{GeV}$ for the leading dijets. Also shown is the analytic 0–jet prediction valid for small μ_R

any BFKL evolution, whether it describes $\gamma^*\gamma^*$, ep, or pp physics.

The iterative approach of [55,56] to solving the BFKL equation at leading-logarithmic accuracy allows not only a study on the partonic level of BFKL in processes with complicated impact factors, where it might be difficult to get analytic expressions for the cross section. The method also allows for the reconstruction of the full final-state configurations contributing to the BFKL evolution, and therefore it is possible to study quantities such as multiplicities and distribution in transverse momentum of the emitted gluons [57]. Only this reconstruction of the full final state allows for the observation of energy and momentum conservation. The effects of energy and momentum conservation have been studied in several processes [58–60]. When no phase space constraints are imposed, the iterative solution reproduces the known analytic solution to the BFKL equation. This iterative approach has recently been generalized [61,62] to solving the NLL BFKL equation thereby joining other approaches [63–67] in studying effects of NLL corrections.

The effects on the total center of mass energy of considering the full multi-gluon BFKL final state in gluon–gluon scattering is seen in Fig. 5. We have plotted the result of considering only the two leading dijets (i.e. ignoring the sum in (20)), and from considering the full BFKL final state (i.e. using the full expression in (20)) (see [57] for more details). Figure 5 shows the average energy for a BFKL dijet event as a function of the rapidity separation of the leading dijets, when the BFKL gluon phase space is unconstrained. The standard analytic solution to the BFKL equation implicitly assumes that all of this phase space is available. It is clear from Fig. 5 that the energy taken up by BFKL radiation is significant compared to the center of mass energy at present and planned colliders. For example at four units of rapidity, which is the upper limit
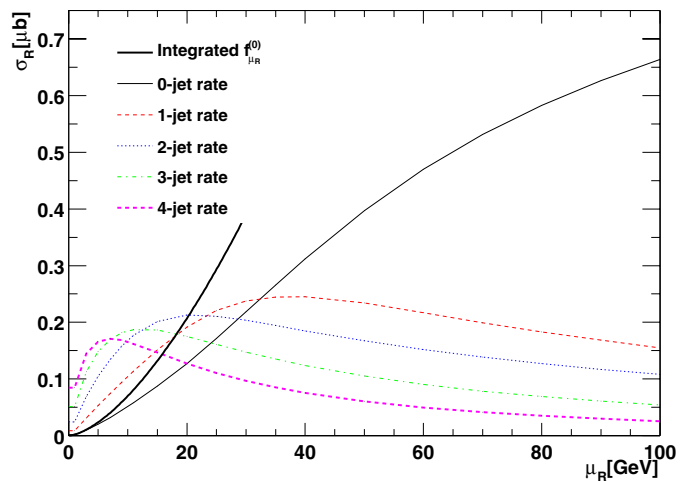
of HERA at present, the average energy of a BFKL dijet event is about $\sqrt{\hat{s}} = 1\,\mathrm{TeV}$ according to Fig. 5, which is far beyond the maximum energy available. At the HERA center of mass energy $\sqrt{\hat{s}} = 300\,\mathrm{GeV}$ the rapidity range would be less than one unit and thus leave very little phase space for additional emissions. Therefore, any constraint on the BFKL radiation from e.g. overall energy conservation will have an impact on BFKL phenomenology predictions at such colliders. In fact, it is found that if energy and momentum conservation is satisfied, by using the full equation (20) when calculating hadronic dijet production at the LHC, then the exponential rise in cross section as a function of the rapidity separation found for gluon–gluon scattering (when the BFKL gluon phase space is integrated to infinity) is moderated to an almost no-change situation compared to the fixed leading order QCD prediction. Other BFKL signatures, like the increasing dijet angular de-correlation with increasing rapidity separation [68–70], are still present.

With the iterative method of solving the LL BFKL equation it is of course also possible to calculate jet rates and transverse momentum distributions (since full information of the final-state configuration is obtained) arising from the BFKL dynamics. Below we present results on the jet rates in gluonic dijet production (on the partonic level, i.e. with the full gluonic phase space assumed in the standard analytic solution of the BFKL equation) with a BFKL chain spanning 5 units of rapidity using a very simple jet definition. We simply let any gluon with a transverse momentum greater than some cutoff μ_R define a jet (this is a reasonable jet definition since at leading-logarithmic accuracy the emitted gluons are well separated in rapidity). These jet rate predictions will change, once the partonic cross section is convoluted with parton density functions. The jet rates of Fig. 6 are the ones responsible for the increase in the center of mass energy of a BFKL event over a simple LO configuration seen in Fig. 5, but they are also responsible for the rise in cross section pre-

dicted from the BFKL dynamics when the BFKL gluonic emission is unbounded. In [57] it is found that for gluon–gluon scattering (with a minimum transverse momentum of the leading dijets of $20\,\mathrm{GeV}$) with a BFKL exchange, one can expect a BFKL gluon emission density of about one hard ($k_{\perp i} > 20\,\mathrm{GeV}$) gluon for every two units of rapidity spanned by the BFKL evolution, when the energy of the event is unconstrained. This amount of radiation is implicitly assumed in the standard analytic solution of the LL BFKL equation.

In conclusion, carefully taking energy-momentum conservation into account dramatically modifies the strong increase for small x, predicted in the leading-log BFKL approach.

3.4 The saturation scale

The parton saturation idea is realized with the help of a non-linear evolution equation in which the gluon splitting is described by a linear term while the negative non-linear term results from the competing gluon recombination (see also [28]). The Balitsky–Kovchegov (BK) equation [71,72] was derived for deep inelastic scattering of a virtual photon on a large nucleus by the resummation of multiple pomeron exchanges in the leading-logarithmic approximation (when $\alpha_{\mathrm{s}} \ln(1/x) \sim 1$ and $x \simeq Q^2/s$) in the large N_c limit. It is an equation for the dipole–proton forward scattering amplitude $N(\mathbf{x}, \mathbf{y}, \mathbf{Y})$ where $\mathbf{x}, \mathbf{y}$ are the end points of the $q\bar{q}$ dipole and $Y = \ln 1/x$ is the rapidity of the process. The BK equation has the following integro-differential form [72]

$$\frac{\partial N(\mathbf{x}, \mathbf{y}, \mathbf{Y})}{\partial Y} = \bar{\alpha}_{\mathrm{s}} \int \frac{\mathrm{d}^2 \mathbf{z} (\mathbf{x} - \mathbf{y})^2}{(\mathbf{x} - \mathbf{z})^2 (\mathbf{y} - \mathbf{z})^2}$$
$$\times [N(\mathbf{x}, \mathbf{z}, \mathbf{Y}) + N(\mathbf{y}, \mathbf{z}, \mathbf{Y}) - N(\mathbf{x}, \mathbf{y}, \mathbf{Y})$$
$$- N(\mathbf{x}, \mathbf{z}, \mathbf{Y}) N(\mathbf{y}, \mathbf{z}, \mathbf{Y})], \qquad (21)$$

where $\bar{\alpha}_{\mathrm{s}} = 3\alpha_{\mathrm{s}}/\pi$ and is fixed in the leading $\ln 1/x$ approximation. The linear term in (21) is the dipole version of the BFKL equation whereas the quadratic term describes the gluon recombination. Instead of $\mathbf{x}, \mathbf{y}$ one often uses their linear combinations: $\mathbf{r} = \mathbf{x} - \mathbf{y}$ which is the size of the dipole and $\mathbf{b} = \frac{1}{2}(\mathbf{x} + \mathbf{y})$ the impact parameter. Equation (21) can be easily solved when using the approximation of the infinitely large nucleus, i.e. assuming that the amplitude $N(\mathbf{x}, \mathbf{y}, \mathbf{Y}) \equiv N(|\mathbf{r}|, \mathbf{Y})$ depends only on the size of the dipole but not on the impact parameter [73–75]. The more complicated case with the full impact parameter dependence has been analyzed recently [76]. For the b-independent and cylindrically symmetric solution, $N(\mathbf{r}, \mathbf{Y}) = N(r, Y)$, (21) can be rewritten in momentum space in a much simpler form after performing the following Fourier transform

$$\phi(k, Y) = \int \frac{\mathrm{d}^2 \mathbf{r}}{2\pi} \exp(-i\mathbf{k} \cdot \mathbf{r}) \frac{N(r, Y)}{\mathbf{r}^2}$$
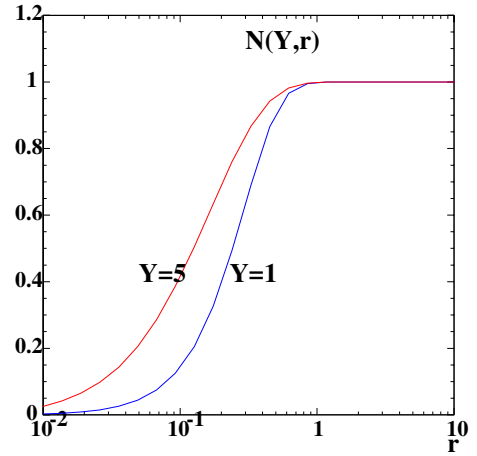$$= \int_0^\infty \frac{\mathrm{d}r}{r} J_0(kr) N(r, Y), \qquad (22)$$

Fig. 7. The amplitude $N(r, Y)$ as a function of the dipole size r for two different rapidities $Y = 1, 5$

where J_0 is the Bessel function. In this case the following equation is obtained:

$$\frac{\partial \phi(k, Y)}{\partial Y} = \bar{\alpha}_{\mathrm{s}} (K \otimes \phi)(k, Y) - \bar{\alpha}_{\mathrm{s}} \phi^2(k, Y). \quad (23)$$

Here the expression $(K \otimes \phi)(k, Y)$ means the action of the usual BFKL kernel in the momentum space onto the function $\phi(k, Y)$. Let us briefly analyze the basic features of $N(r, Y)$ and $\phi(k, Y)$. In Fig. 7 we plot the amplitude $N(r, Y)$ as a function of the dipole size r for different values of rapidity Y. The amplitude $N(r, Y)$ is small for small values of the dipole size. It is governed in this regime by the linear part of (21). For larger values of dipole sizes, $r > 1/Q_s(Y)$, the amplitude grows and saturates eventually to 1. This is the regime where the non-linear effects are important. As it is clear from Fig. 7 the saturation scale grows with rapidity $Q_s(Y)$. This means that with increasing rapidities the saturation occurs for smaller dipoles. It has been shown that the growth of the saturation momentum is exponential in rapidity $Q_s(Y) = Q_0 \exp(\lambda Y)$ with $\lambda \simeq 2\bar{\alpha}_{\mathrm{s}}$ being a universal coefficient and governed by the equation. The normalization Q_0 on the other hand is dependent on the initial condition $N(r, Y = 0)$. We note however, that when the rapidity Y is not too large the initial conditions are still important. In this region the coefficient λ can still depend on the rapidity [74].

It has to be stressed that in the leading-log x approximation the strong coupling constant is fixed. The running of the coupling, although being a next-to-leading-log x effect, is obviously more physical. In this case the rapidity dependence of the saturation scale is changed. We adopt a natural approximation that the local exponent of the saturation scale $\lambda(Y) = \mathrm{d} \ln(Q_s(Y)/\Lambda)/\mathrm{d}Y$ takes the form $\lambda(Y) = 2\bar{\alpha}_{\mathrm{s}}(Q_s^2(Y))$ where $\Lambda = \Lambda_{\mathrm{QCD}}$. The above form is motivated by the leading-logarithmic result with the fixed coupling as discussed before, i.e. $Q_s(Y) = Q_0 \exp(\lambda Y)$.

Thus, we have

$$\frac{\mathrm{d} \ln(Q_s(Y)/\Lambda)}{\mathrm{d}Y} = \frac{12}{b_0 \ln(Q_s(Y)/\Lambda)}, \qquad (24)$$
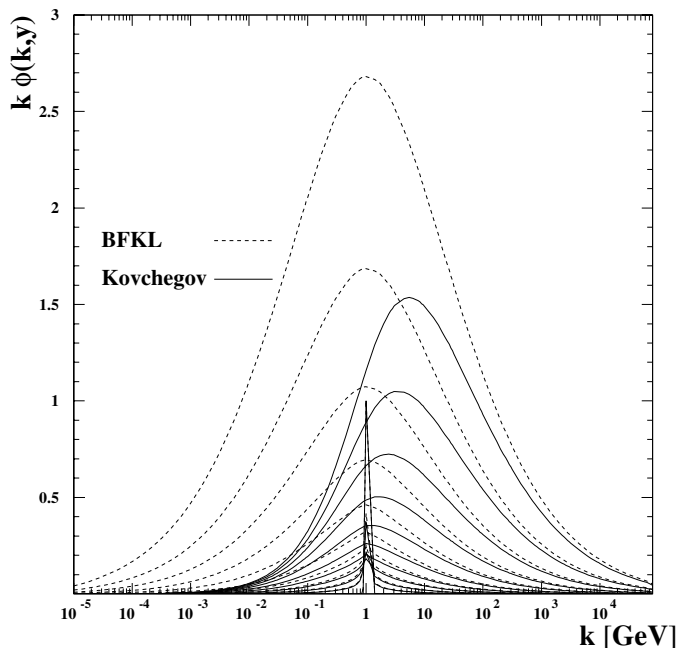
Fig. 8. The Fourier transform of the amplitude $N(r, Y)$ as a function of the momentum k for different values of rapidities Y increasing from 1 to 10. Dashed lines correspond to the solution to the BFKL equation whereas solid lines to the full non-linear BK equation

with the initial condition $Q_s(Y_0) = Q_0$ and Y_0 chosen in the region where scaling sets in. The solution takes the form

$$Q_s(Y) = \Lambda \, \exp\left(\sqrt{\frac{24}{b_0}(Y - Y_0) + L_0^2}\right), \qquad Y > Y_0 \,,$$
(25)

where $L_0 = \ln(Q_0/\Lambda)$. Thus, the exponential dependence on the rapidity Y of the saturation scale is changed in the running coupling case to the milder behavior [75]. In the phenomenological analysis of the HERA data based on the BK equation [77], the running of the α_s has been included. It has been shown that, in the limited range of x, the effective power governing the behavior of the saturation scale can be still fitted using the simple form $Q_s(Y) \sim \exp(\lambda_0 Y)$ with $\lambda_0 \simeq 0.18$, which is close to the value used in the Golec-Biernat and Wüsthoff saturation model [78,79].

In what follows we consider the solution to the Balitsky–Kovchegov equation in the leading-log x fixed coupling case. In Fig. 8 we plot the solution $k\phi(k, Y)$ in momentum space as a function of k for increasing rapidities. We have imposed the initial condition of the form of the delta function, localized at some $k = k_0 = 1$ GeV. We compare the solution of the BK equation with that of the linear BFKL which exhibits the strong unlimited diffusion into both infrared and ultraviolet regimes. The BFKL solution is symmetric and peaked around the initial value $k = k_0$. The solution to the BK equation shows on the other hand a suppression of the diffusion into the low momenta. We clearly see that the peak of the distribution moves with increasing rapidity to the higher momenta. One can identify the value of the momentum k at which the maximum occurs as the saturation

scale $Q_s(Y)$. At large momenta k where the non-linearity in the BK equation does not play a role, the two solutions BFKL and BK are close to each other. The overall height of the distribution is strongly damped with respect to the linear case.

The solution to the BK equation shows also another interesting feature, namely the property of scaling (e.g. [75, 80, 81]). In the non-linear regime $r > 1/Q_s(Y)$ the amplitude depends only on one combined variable instead of r and Y separately,

$$N(r, Y) \equiv N(r \, Q_s(Y)). \tag{26}$$

This is also property of the GBW saturation model, though in the latter case the scaling was present for all values of r. In the case of BK equation, scaling only occurs in the saturation domain that is for large values of dipole sizes.

3.5 Non-linear evolution versus HERA data

A new approach to a global QCD analysis based on the non-linear QCD evolution by Balitsky–Kovchegov (BK) is presented in [74, 77]. The BK equation improved by the DGLAP corrections for small dipole sizes (independently of impact parameter) is in fact very successful in describing the low x part of the structure function F_2 at HERA. In the following a brief summary of the results in [77] is given.

With the initial conditions specified at $x_0 = 10^{-2}$ the BK equation (without impact parameter dependence) is solved numerically towards smaller x. The impact parameter dependence is restored using a rescattering ansatz of the Glauber type. All existing low x ($x \leq 0.01$) data on the F_2 structure function are reproduced with resulting $\chi^2/\mathrm{ndf} \simeq 1$ (Fig. 9). Only two parameters and a few fixed ones (associated with the initial conditions) are used for the fit. The fitted parameters are the effective proton radius, entering the Gaussian impact parameter distribution, and the scale at which the DGLAP corrections are switched on ($\mathcal{O}(1\,\mathrm{GeV})$). The DGLAP corrections are important for large photon virtualities only and reach up to 15%. The low Q^2 (of the order of a few GeV^2 and below) data are described solely by the BK equation.

In DIS the pomeron intercept is obtained by a measurement of $\lambda \equiv \mathrm{d}\ln F_2/\mathrm{d}\ln(1/x)$. For large photon virtualities the fit based on the BK equation reproduces the HERA data with $\lambda \simeq 0.3$–0.4, the hard BFKL intercept. In the small-Q^2 region the non-linear terms in the BK equation are reflected in the smaller λ values at smaller Q^2. Figure 10 presents a prediction for λ at at smaller Q^2 and smaller x. Figure 11 presents results for $x \stackrel{>}{\sim} 10^{-4}$. In this region λ decreases strongly for small Q^2 but varies relatively slowly with x. In Fig. 10 we see, however, that for smaller values of x, λ decreases more strongly with x, for fixed Q^2, tending to zero in agreement with the unitarity constrain. At Q^2 well below 1 GeV^2 and $x \simeq 10^{-6}$, $\lambda \simeq 0.08$–0.1. This value of λ coincides with the "soft pomeron" intercept. Thus the non-linear evolution provides a solution to the problem of hard–soft pomeron transition.
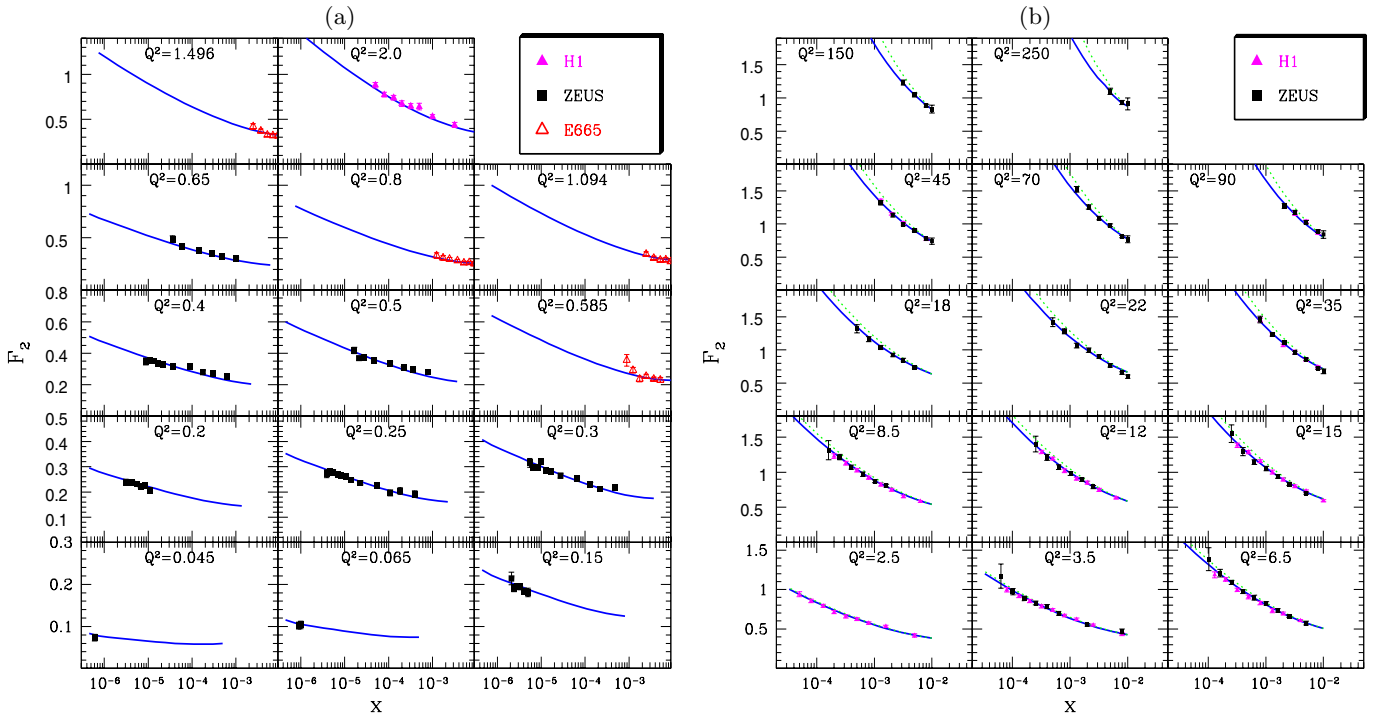
Fig. 9. Fit to the F_2 structure function. The dashed line is a result obtained without the DGLAP corrections. The data are from [45, 82–84]

The main fitting parameter used for the fit is an effective proton radius R. The optimal fit is achieved at $R \simeq 0.3\,\text{fm}$, the radius which is much smaller than the electro-magnetic radius of the proton. On the one hand, this small proton radius might be an artifact of the approximations used. On the other hand, it may indeed indicate a small size dense gluon spot inside the proton. Such a scenario arises in several other models for high-energy scattering off proton [85, 86].

The approach based on non-linear QCD evolution allows the extrapolation of the parton distributions to very high energies available at the LHC as well as very low photon virtualities, $Q^2 \ll 1\,\text{GeV}^2$.

3.6 Multiple interactions in non-ordered cascades

At high energies the perturbative jet cross section in pp collisions becomes larger than the total cross section. This implies that there are often several hard sub-collisions in a single event. Therefore correlations become important, and the observed "pedestal effect" implies that the hard sub-collisions are not independent [87], indicating an impact parameter dependence such that central collisions have many mini-jets, while peripheral collisions have fewer mini-jets [87]. Also at HERA the final-state properties in photoproduction cannot be reproduced without assuming multiple hard scattering [88–90]. At higher Q^2 the indications for multiple scattering are reduced, and thus HERA offers a unique possibility to study how, with decreasing Q^2, multiple interactions become more and more impor-
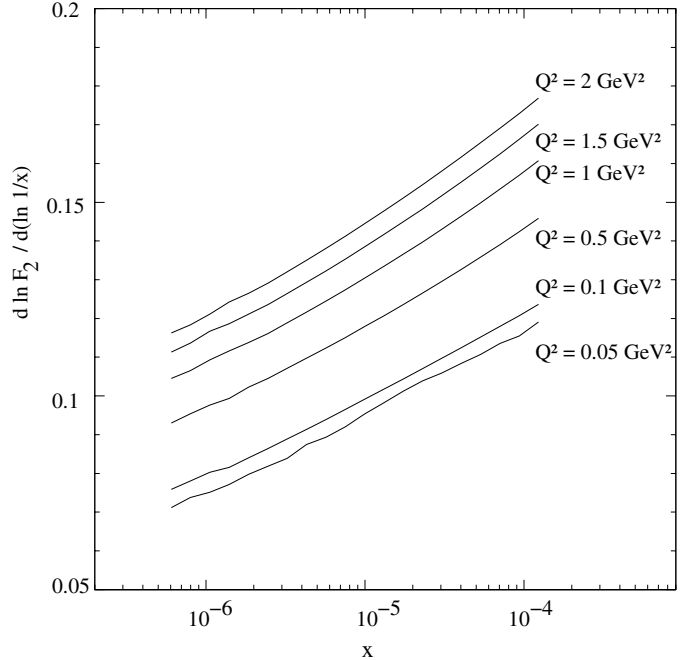

Fig. 10. The logarithmic derivative $\lambda = \partial \ln F_2 / \partial \ln 1/x$ plotted at low Q^2 and very low x

tant, until eventually a situation similar to pp collisions is reached for $Q^2 = 0$.

In a non-$k_\perp$-ordered BFKL ladder, it is possible to have two (or more) local $k_\perp$-maxima, which then correspond to two different hard sub-collisions. Thus there are two
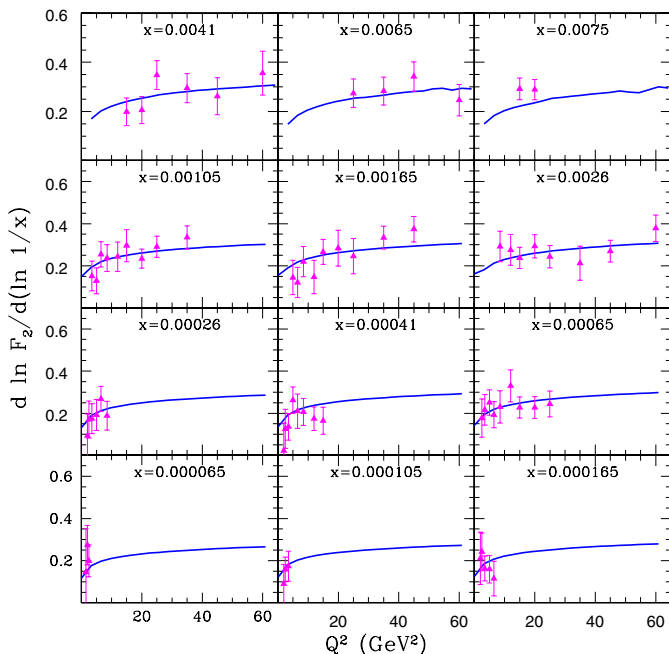
Fig. 11. The logarithmic derivative $\lambda = \partial \ln F_2 / \partial \ln 1/x$ as a function of Q^2 for different values of x

different sources for multiple interactions: It is possible to have two hard scatterings in the same chain, and there may be more than one chain in a single event. The BFKL, CCFM or LDC formalism can be used to estimate multiple collisions in a single chain. The symmetric properties of the LDC model for DIS makes it especially suited to be applied to pp collisions, and in [91] it is demonstrated that it is possible to deduce the average number of chains in pp scattering from data on deep inelastic ep scattering.

The LDC model can, however, not determine the correlations between the chains. Uncorrelated chains would be described by a Poissonian distribution, but the observed pedestal effect, mentioned above, makes it more likely that central collisions have more, and peripheral collisions fewer, chains. The analysis by Sjöstrand and von Zijl [87] favors an impact parameter dependence described by a double Gaussian distribution. It turns out that this distribution leads to a geometric distribution in the number of sub-collisions, with the tail suppressed by energy conservation. Some predictions for mini-jet multiplicity and the pedestal effect in pp collisions are presented in [87], assuming such a geometric distribution for the number of chains in a single pp event. Further work is in progress, and it would be very interesting to test these ideas, not only in pp or $p\bar{p}$ collisions, but also in ep scattering, varying Q^2 from the DIS region to photoproduction.

3.7 Spin dependent unintegrated parton distributions

The basic, universal quantities which describe the inclusive cross sections of hard processes within the QCD improved parton model are the scale dependent parton distributions. These parton distributions or distribution amplitudes de-

scribe how the momentum of the nucleon is distributed among its constituents, i.e. quarks and gluons.

Polarized parton distributions are a probabilistic measure for the distribution of the nucleon's longitudinal spin (helicity) among its constituents. More precisely, one defines polarized parton distributions as the difference of the probability density to find a parton f with its longitudinal spin parallel aligned minus the probability density to find the same parton with its longitudinal spin antiparallel aligned relative to the spin of the nucleon:

$$\Delta f = f_{\uparrow\uparrow} - f_{\uparrow\downarrow} \ . \qquad (27)$$

These parton distributions conventionally only depend on x and Q^2, but just as for the spin independent case it may be beneficial to also consider $k_\perp$-unintegrated polarized parton distributions. An evolution equation analogous to CCFM has been derived for the unintegrated gluon distribution in [92] and the result is quite similar, although contrary to the unpolarized case there is no non-Sudakov form factor since the polarized splitting function does not have a $1/z$ pole.

One can show that the principles discussed in [92] with slight modifications also apply for the case of including quarks in the evolution. Thus one arrives at a complete set of evolution equations along the lines of CCFM for the unpolarized case. The CCFM evolution for polarized gluons is called the pCCFM evolution equation [93].

It can easily be shown that in the small-x limit the pCCFM equation formulated in [92] generate the double[7] $\ln^2(1/x)$ for distributions integrated over transverse momentum of the partons. Their detailed structure is however different from the collinear QCD expectations [94,95]. One can modify the pCCFM equations in order to incorporate those expectations and make contact with the evolution equations in the integrated case containing Altarelli–Parisi + ladder contributions which have been discussed in [94]. These modifications contain the following steps [93].

(1) In order to get the expected double logarithmic limit of the integrated distributions it is sufficient to replace the angular ordering constraint $\Theta(Q - z|\mathbf{q}_\perp|)$ by the stronger constraint $\Theta(Q^2 - zq_\perp^2)$ in the corresponding evolution equations for integrated distributions.

(2) The argument of α_s will be set equal to $q_\perp^2$ instead of $q^2 \equiv q_\perp^2(1-z)^2$.

(3) The non-singular parts of the splitting function(s) will be included in the definition of the Sudakov form factor(s).

(4) Following [94] we include the complete splitting functions $P_{ab}(z)$ and not only their singular parts at $z = 1$ and constant contributions at $z = 0$.

(5) We represent the splitting functions $\Delta P_{ab}(z)$ by $\Delta P_{ab}(z) = \Delta P_{ab}(0) + \Delta \bar{P}_{ab}(z)$, where $\Delta \bar{P}_{ab}(0) = 0$.

Following [94] we shall multiply $\Delta P_{ab}(0)$ and $\Delta \bar{P}_{ab}(z)$ by $\Theta(Q^2 - zq_\perp^2)$ and $\Theta(Q^2 - q_\perp^2)$ respectively in the integrands of the corresponding integral equations. Following the terminology of [94] we call the corresponding contributions to the evolution kernels the "ladder" and "Altarelli–Parisi" contributions respectively.

---

[7] The double $\ln^2(1/x)$ terms come from non-ladder bremsstrahlung terms.

(6) We shall "unfold" the eikonal form factors in order to treat real emission and virtual correction terms on an equal footing.

After those modifications one arrives at an evolution equation for the unintegrated polarized parton distributions which includes the complete LO Altarelli–Parisi and the double $\ln^2(1/x)$ effect generated by ladder diagrams in a consistent way, i.e. if one integrates the evolved unintegrated parton distributions over the transverse momentum $k_\perp$ the result will be the same as if one had done an evolution with the integrated parton distributions using the "Altarelli–Parisi + ladder" evolution equation. This means that the corresponding diagram between evolution and transverse momentum integration commutes.

One can utilize the fact that the pCCFM equation can be (partially) diagonalized by the Fourier–Bessel transform. It turns out that the difference between the integrated and the unintegrated evolution equation in Fourier-space is only a single factor $J_0(b_\perp q_\perp(1-z))$, where $b_\perp$ is the transverse impact parameter conjugate to the transverse momentum of the parton, $q_\perp$ the transverse evolution scale, z the momentum fraction and J_0 the Bessel function of order 0. The evolution equation for the integrated case is simply restored by setting $b_\perp = 0$.

There is a third contribution to the evolution of unintegrated polarized parton distributions which is not covered by the "Altarelli–Parisi + ladder" approximation of the modified pCCFM equation; these are the non-ladder bremsstrahlung contributions. A general method of implementing the non-ladder bremsstrahlung corrections into the double logarithmic resummation was proposed by Kirschner and Lipatov [96,97]. For unintegrated polarized parton distributions they have been implemented in [94]. In the unintegrated case one can simply add them by analogy to the Altarelli–Parisi and ladder contribution by inserting the factor $J_0(b_\perp q_\perp(1-z))$ because then again one obtains perfect commutativity of the diagram between the integrated and unintegrated parton distributions.

Putting all three contributions together (Altarelli–Parisi, ladder + non-ladder) one obtains a set of linear integral equations for unintegrated polarized quark and gluon distributions. In Fig. 12 we show the evolution of the $k_\perp$ dependence for the triplet contribution:

$$\Delta f_3 = \frac{1}{6} \left(\Delta u + \Delta \bar{u} - \Delta d - \Delta \bar{d} \right). \tag{28}$$

The input distributions at $Q_0^2 = 0.26\,\mathrm{GeV}^2$ are taken from [98,99] and are compared to the evolved distributions at $Q^2 = 10.0\,\mathrm{GeV}^2$. The width of the initial transverse momentum dependence σ has been chosen to be $1\,\mathrm{GeV}$. For the simulation the Altarelli–Parisi, ladder and non-ladder contributions all have been included. It is seen that due to the evolution the $k_\perp$ dependence is broadening away from a Gaussian behavior to a more exponential decay.

3.8 J/ψ production and polarization effects

In the following we consider J/ψ meson production in ep deep inelastic scattering in the color-singlet model using
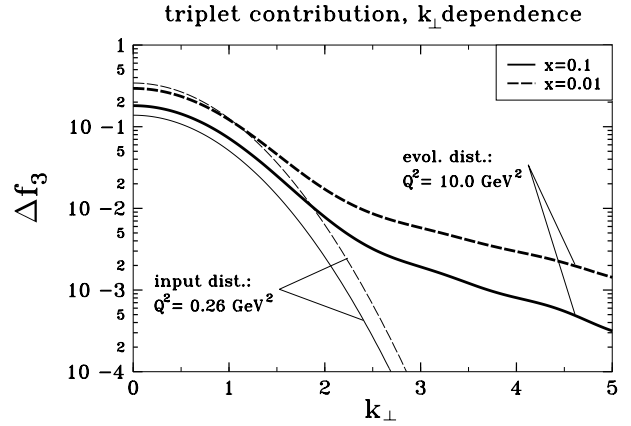

Fig. 12. Transverse momentum dependence for the triplet contribution $\Delta f_3 = \frac{1}{6} \left(\Delta u + \Delta \bar{u} - \Delta d - \Delta \bar{d} \right)$ using pCCFM evolution including non-ladder contributions. The thin lines show the input distributions for $Q_0^2 = 0.26\,\mathrm{GeV}^2$ for $x = 0.1$ (solid) and $x = 0.01$ (dashed), while the bold lines show the same distribution evolved to $Q^2 = 10\,\mathrm{GeV}^2$

$k_\perp$-factorization. It should be noted that heavy quark and quarkonium cross section calculations within the collinear factorization in fixed-order pQCD show a large discrepancy (by more than an order of magnitude) [100–103] to measurements at the Tevatron for hadroproduction of J/ψ and Υ mesons. This fact has resulted in intensive theoretical investigations of such processes. In particular, it was suggested to add an additional transition mechanism from $c\bar{c}$-pairs to J/ψ mesons, the so-called color octet (CO) model [104], where a $c\bar{c}$-pair is produced in a color octet state and transforms into the final color-singlet (CS) state by the help of very soft gluon radiation. The CO model is based on the general principle of the non-relativistic QCD factorization [104]. The physics behind this factorization is simple: the heavy quark–antiquark meson is produced at distances which are not so short as the distances for heavy quark–antiquark production (which are of the order of $1/2m_Q$, where m_Q is the mass of the heavy quark). Indeed, we can easily estimate that the typical distances for e.g. J/ψ production is about $1/\alpha_s(m_Q)m_Q$. These distances are much longer than the distances of the typical hard process, but they are still much shorter than the hadronization distances. Therefore J/ψ production is still under control of perturbative QCD, but on the other hand it could be accompanied by a highly non-perturbative production of soft gluons. By adding the contribution from the CO model and fitting the free parameters one was able to describe the existing data on J/ψ production at the Tevatron. However, in recent years, we have seen a lot of difficulties of the CO model. The first and the most disturbing one is the fact that the fit with the CO model gives values of wave functions at the origin which are in contradiction with the non-relativistic (NR) QCD hierarchy where each non-perturbative CO matrix element has a definite order of magnitude in the relative heavy quark velocity. The qualitative prediction for the CO model is the transverse polarization of the produced J/ψ since the main contribution of the CO model to J/ψ production in $p\bar{p}$
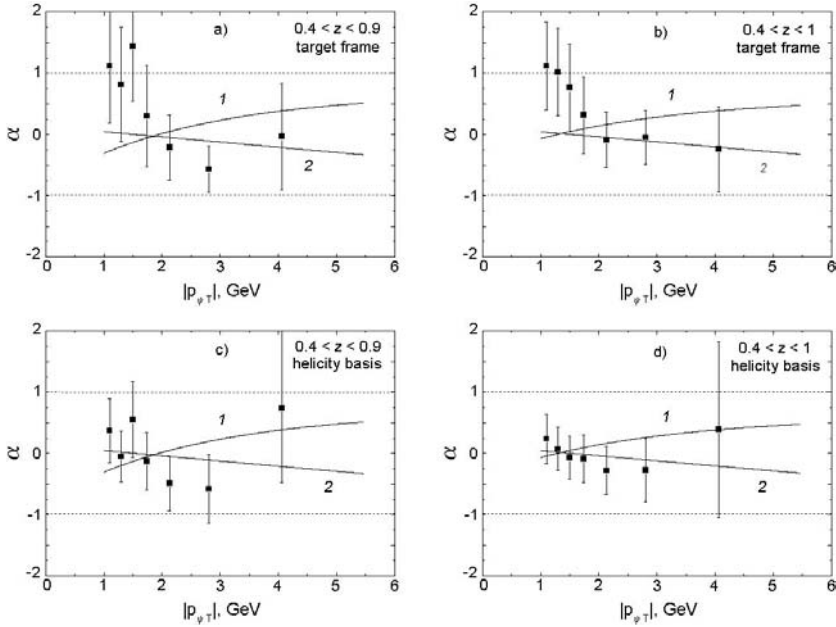
Fig. 13. The spin alignment parameter $\alpha(p_{\perp,\psi})$, which is calculated in the region $0.4 < z < 0.9$ (**a** and **c**) and in the region $0.4 < z < 1$ (**b** and **d**) at $\sqrt{s} = 314\,\text{GeV}$, $m_c = 1.4\,\text{GeV}$ and $\Lambda_{\text{QCD}} = 250\,\text{MeV}$. Curves *1* corresponds to calculations in the collinear approach at leading order with the GRV gluon density, curves *2* corresponds to the $k_{\perp}$-factorization calculations with the **JB** unintegrated gluon distribution

collisions comes from gluon–gluon fusion with transverse polarized gluons. The second important question is about the NR QCD factorization itself. Is the heavy quark mass really large enough to have well separated scales, $1/2m_Q$ and $1/2\alpha_{\text{s}}(m_Q)m_Q$, or is a special selection needed as suggested in [105] The CO model has been applied earlier in the analysis of inelastic J/ψ production [106, 107] at HERA. However, as noted in [107], the results from [106,107] do not agree with each other. Also the results obtained within the usual collinear approach and the CS model [108–111] underestimate the experimental data by a factor of about two.

First attempts to investigate the J/ψ polarization problem in ep-interactions at HERA and in $p\bar{p}$-interactions at the Tevatron were made in [112–116] using the $k_{\perp}$-factorization approach. An extensive analysis of the production of J/ψ, χ_c and Υ mesons (including the polarization properties) in $p\bar{p}$ collisions has been recently presented in [117].

The matrix element for DIS electro-production of J/ψ mesons has been calculated in [118], keeping the full Q^2 dependence as well as the full polarization state of the J/ψ meson. For studying J/ψ meson polarization properties we calculate the $p_{\perp,\psi}$- and Q^2-dependences of the spin alignment parameter α [19, 61]:

$$\alpha(\omega) = \frac{\mathrm{d}\sigma/\mathrm{d}\omega - 3\,\mathrm{d}\sigma_{\text{L}}/\mathrm{d}\omega}{\mathrm{d}\sigma/\mathrm{d}\omega + \mathrm{d}\sigma_{\text{L}}/\mathrm{d}\omega}, \qquad (29)$$

where σ (σ_{L}) is the production cross section for (longitudinally polarized) J/ψ mesons and with $p_{\perp,\psi}$ or Q^2 substituting ω. The parameter α controls the angular distribution for leptons in the decay $J/\psi \to \mu^+ \mu^-$ (in the J/ψ meson rest frame):

$$\frac{\mathrm{d}\Gamma(J/\psi \to \mu^+ \mu^-)}{\mathrm{d}\cos\theta} \sim 1 + \alpha\cos^2\theta. \qquad (30)$$

Figure 13 shows the spin alignment parameter $\alpha(p_{\perp,\psi})$ calculated in the region $0.4 < z < 0.9$ (a) and $0.4 < z < 1$

(b), with $z = E_\psi/E_\gamma$ in the p-rest frame, in comparison with experimental data taken by the ZEUS collaboration at HERA [119]. Curves *1* correspond to calculations in the collinear approach at leading order using the GRV gluon density, curves *2* correspond to the $k_{\perp}$-factorization calculations with the BFKL **JB** [120] unintegrated gluon distribution with $Q_0^2 = 1\,\text{GeV}^2$.

We note that it is impossible to make definite conclusions about the $k_{\perp}$-factorization approach considering the polarized J/ψ production cross section because of the large uncertainties in the experimental data. The large additional contribution from the initial longitudinal polarization of virtual photons weakens the effect of initial gluon off-shellness even more. However at low $Q^2 < 1\,\text{GeV}^2$ such contributions are negligible. This fact should result in observable spin effects of the final J/ψ mesons. As an example, we have performed calculations for the spin alignment parameter α as a function of $p_{\perp,\psi}{}^2$ at fixed values of Q^2 for $40\,\text{GeV} \le W \le 180\,\text{GeV}$, $z > 0.2$, $M_X \ge 10\,\text{GeV}$ at HERA.

The results of our calculations at fixed values of $Q^2 = 0.1, 1, 5, 10\,\text{GeV}^2$ are shown in Fig. 14. Curves *1* correspond to calculations in the collinear approach at leading order using the GRV gluon density and curves *2* correspond to the $k_{\perp}$-factorization calculations with the **JB** unintegrated at $Q_0^2 = 1\,\text{GeV}^2$. We observe large differences between predictions of the leading order of the color-singlet model with the GRV gluon density and the $k_{\perp}$-factorization approach at low $Q^2 < 1\,\text{GeV}^2$ (Fig. 14).

Therefore more accurate measurements of polarization properties of the J/ψ mesons will be an interesting test of the $k_{\perp}$-factorization approach.

For the production of J/ψ particles in the framework of the CS model the relevant partonic subprocess is
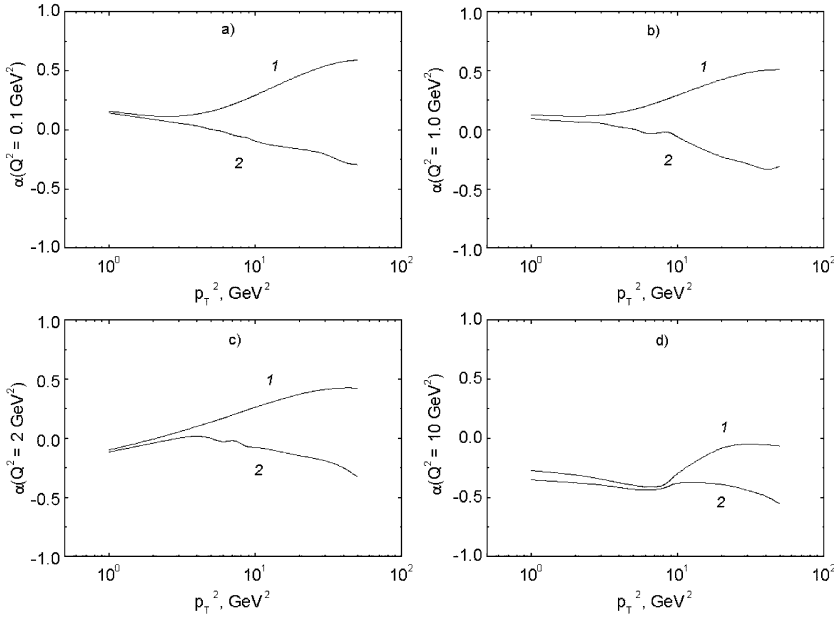
$$\gamma + g \to {}^3S_1[1] + g. \qquad (31)$$

Fig. 14. The spin alignment parameter $\alpha(p_{\perp,\psi}^2)$ at fixed values of Q^2 for $40\,\text{GeV} \leq W \leq 180\,\text{GeV}$, $z > 0.2$, $M_X \geq 10\,\text{GeV}$ at $\sqrt{s} = 314\,\text{GeV}$, $m_c = 1.4\,\text{GeV}$ and $\Lambda_{\text{QCD}} = 250\,\text{MeV}$. Curves 1 and 2 correspond to the calculations as in Fig. 12
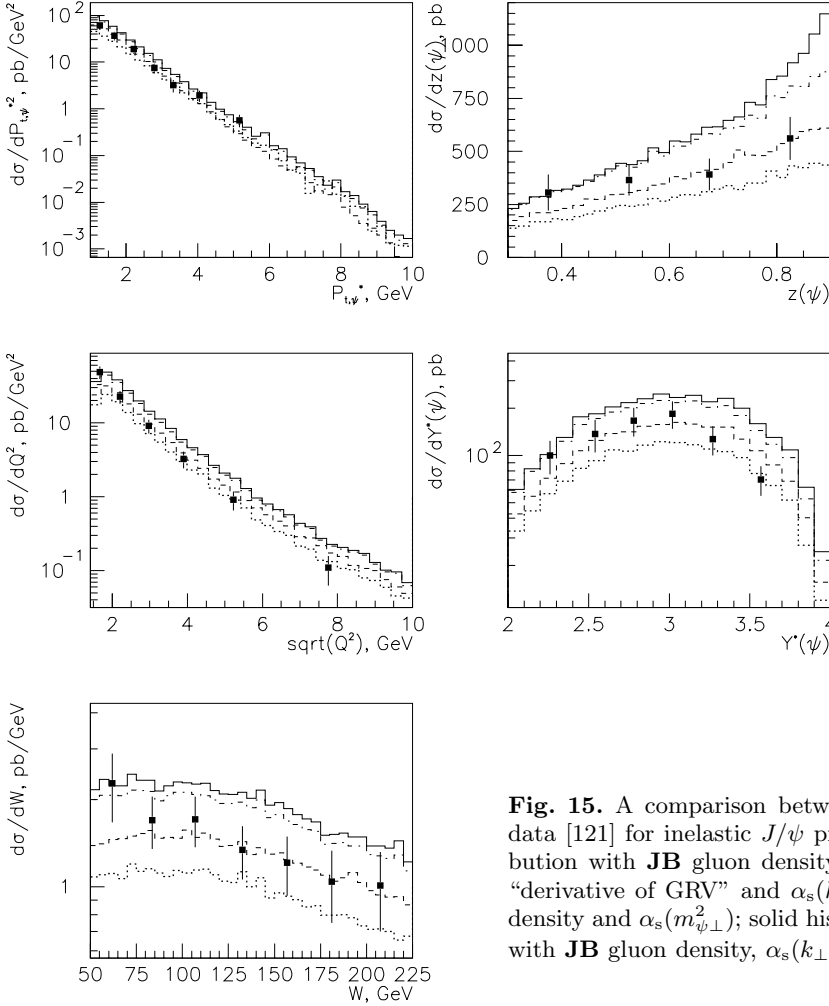

Fig. 15. A comparison between the theoretical predictions and experimental data [121] for inelastic J/ψ production. Dash-dotted histogram, the CS contribution with **JB** gluon density and $\alpha_s(k_\perp^2)$; dashed histogram, the same with "derivative of GRV" and $\alpha_s(k_\perp^2)$; dotted histogram, the same with **JB** gluon density and $\alpha_s(m_{\psi\perp}^2)$; solid histogram, the sum of the CS and CO contributions, with **JB** gluon density, $\alpha_s(k_\perp^2)$

When the CO $q\bar{q}$ states are allowed, there appear additional contributions from the following partonic subprocesses:

$$\gamma + g \to {}^1S_0[8] + g, \; {}^3S_1[8] + g, \; {}^3P_J[8] + g. \quad (32)$$

The CO matrix elements responsible for the non-perturbative transitions in (31) are related to the fictitious CO wave functions, that are used in calculations instead of the ordinary CS wave functions. In Fig. 15 we present a comparison between our theoretical calculations and experimental data collected by the H1 collaboration at HERA [121] in the kinematic range $2\,\mathrm{GeV}^2 < Q^2 < 100\,\mathrm{GeV}^2$, $50\,\mathrm{GeV} < W < 225\,\mathrm{GeV}$, $0.3 < z < 0.9$, $p_{\mathrm{T},\psi}^{*\,2} > 1\,\mathrm{GeV}^2$.

The effect of the different evolution equations (BFKL **JB** or DGLAP "derivative of GRV"; for a detailed description see [1]) which govern the evolution of gluon densities is found to be as large as a factor of 2 in the production cross section. This is illustrated by a comparison of dash-dotted and dashed histograms in Fig. 15. A similar effect is connected with the renormalization scale μ_{r}^2 in the running coupling constant $\alpha_{\mathrm{s}}(\mu_{\mathrm{r}}^2)$. The calculations made with $\mu_{\mathrm{r}}^2 = k_\perp{}^2$ and $\mu_{\mathrm{r}}^2 = m_{\psi\perp}^2$ are represented by the dash-dotted and dotted histograms in Fig. 15. Note that the setting $\mu_{\mathrm{r}}^2 = k_\perp{}^2$ is only possible in the $k_\perp$-factorization approach. In this case, $\alpha_{\mathrm{s}}(k_\perp)$ was fixed at $\alpha_{\mathrm{s}}{=}1$ if the formal running value was greater than 1, and it was set to zero if $k_\perp < \Lambda_{\mathrm{QCD}}$. The contributions from the $2 \to 1$ CO subprocesses are cut away by the experimental restriction $z < 0.9$. Turning to the $2 \to 2$ CO contributions, one has to take care about the infrared instability of the relevant matrix elements. In order to restrict the $2 \to 2$ subprocesses to the perturbative domain, we introduce the regularization parameter q_{reg}^2. The numerical results shown in Fig. 15 are obtained with setting $q_{\mathrm{reg}}^2 = 1\,\mathrm{GeV}^2$ and $m_c = m_\psi/2 = 1.55\,\mathrm{GeV}$.

The results shown in Fig. 15 are obtained with the non-perturbative CO matrix elements of [103]. If the values extracted from the analysis [117] were used instead, the contribution from the CO states would be a factor of 5 lower. One can see that, irrespective to the particular choice of the non-perturbative matrix elements, the production of J/ψ mesons at the HERA is reasonably described within the color-singlet production mechanism (with $k_\perp$-factorization) and the color octet contributions are not needed.

4 Selected topics on the current experimental status

In spite of the fact that QCD has been extremely successful in describing the physics at $Q^2 \gg \Lambda_{\mathrm{QCD}}$, the total cross section in deep inelastic scattering (DIS) is dominated by soft and semi-hard processes which cannot be described by perturbative QCD. It is thus of fundamental importance to provide experimental measurements which may give hints to how these processes can be described within the QCD framework.

One of the long standing questions in high-energy collisions is whether significant deviations from the successful
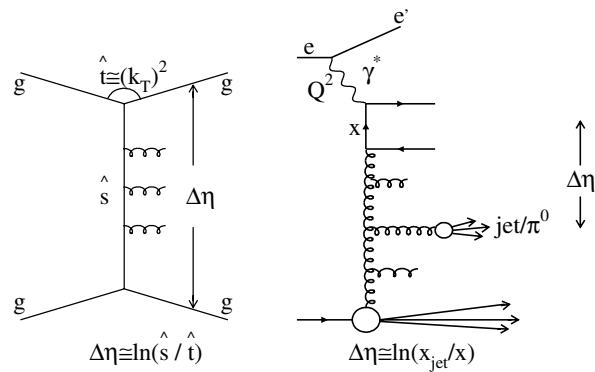

Fig. 16. Kinematics of hard emissions for dijets with large rapidity separation in hadron–hadron collisions (left) and for forward jets/particles at HERA. The maximal measurable jet separation at the Tevatron is about six rapidity units

DGLAP [8–11] evolution equations can be observed at the HERA and/or Tevatron colliders. A fundamental question is where DGLAP evolution breaks down and emissions, not ordered in virtuality, play a significant role. In deep inelastic scattering processes (DIS) at low values of Bjorken variable x it is assumed that the struck parton results from a long cascade of parton branchings. Similarly, in hadron–hadron collision processes where two jets are separated by a large rapidity interval $\Delta\eta$ one expects a long partonic cascade between them (see Fig. 16).[8] At sufficiently low values of x (high values $\Delta\eta$) the DGLAP approximation should fail while the BFKL and CCFM approximations should be applicable.

Calculations of inclusive quantities like the structure function $F_2(x, Q^2)$ at HERA, performed in NLO DGLAP, are in very good agreement with the measurements [83, 176].[9] However the interplay of non-perturbative (input starting distribution) and the perturbative (NLO DGLAP evolution) elements in this calculation makes it impossible to decide if parton cascades with strongly ordered transverse momenta are the dominant mechanism leading to scaling violations.

When exclusive quantities are investigated, the agreement between NLO coefficient functions convoluted with NLO DGLAP parton densities and the data is less satisfactory, and for some processes the DGLAP based theory fails completely. One example is the cross section of forward going jets at HERA, which will be discussed below. The question therefore is, for which observables the next order in the perturbative expansion is enough, and for which a resummation to all orders is needed.

The forward jet production cross section at small Bjorken variable x at HERA and the cross section for jet production with large rapidity separation in high-energy hadron–hadron collisions (Tevatron) have since long been

---

[8] Large rapidity interval events in hadron–hadron collisions correspond to a subclass of DIS events at small x characterized by presence of the forward jet with $x_{\mathrm{jet}} = p_{\mathrm{jet}}/p_{\mathrm{proton}} \gg x$ and transverse momentum $p_{\mathrm{T}} \approx Q$. For such events rapidity interval between forward jet and struck quark $\Delta\eta \approx \ln(x_{\mathrm{jet}}/x) \gg 1$.

[9] The longitudinal structure function $F_{\mathrm{L}}(x, Q^2)$ at small values of Q^2 is an exception; see Sect. 4.1.1

advertised as an ideal test of the perturbative dynamics [53, 70, 177–179]. More refined theoretical and phenomenological analyses have shown that these tests are not so decisive and straightforward; however, they remain in the center of experimental activity of small-x physics. Several measurements of highly energetic jets ($x_{\text{jet}} = E_{\text{jet}}/E_p \gg x$) at large pseudo-rapidities[10] η_{lab} with transverse energies squared $E_{\text{T,jet}}^2$ of the order of Q^2 have been made by both the H1 [149, 151] and the ZEUS collaborations [150, 152]. This kind of measurement, originally proposed by Mueller and Navelet (so-called *Mueller–Navelet forward jets* [53, 177, 178]) is designed such that DGLAP evolution in transverse momentum space is suppressed ($E_{\text{T,jet}} \approx Q$) while BFKL evolution in x-space ($x_{\text{jet}} \gg x$) is enhanced. The measurements showed large discrepancies to DGLAP NLO dijet calculations at low values of Bjorken variable x, which was taken as an indication of the breakdown of the DGLAP approximation and the onset of BFKL effects. However, in the NLO dijet calculations the scale uncertainties are very large. It was also shown [154] that a good description of the data can be obtained by considering the partonic structure of the virtual photon, which is expected to be important for $E_{\text{T,jet}}^2 > Q^2$ and Q^2 not too large. In this approach we are back to the classic DGLAP approximation, with simultaneous evolution in transverse momentum space from both the photon and the proton sides towards the hard scatter and this approach should be relevant if chains with at most one local maximum in tranverse momentum dominate. H1 [151, 156] also measured single forward particles (π^0) as opposed to jets, allowing the study of angles closer to the proton direction and smaller Bjorken variable x, at the price of a stronger dependence on the fragmentation process. Studies of the inclusive cross section for the production of forward particles led essentially to the same conclusions as the study of forward jets.

Studies of the transverse energy flow provide a complementary means of investigating QCD processes. Compared with jet and leading particle studies, measurements of transverse energy flow are sensitive to parton emissions of lower transverse momentum and to the modeling of both the perturbative QCD evolution and the soft hadronization process. In [156] both types of measurement (forward particle and energy flow) have been merged. The transverse energy flow measured for events with forward π^0 reveals the range over which the transverse momentum of the forward parton is compensated. We may expect that different models of parton evolution lead to different radiation patterns.

At first look the measurements of the Mueller–Navelet jets and jet azimuthal de-correlation at the Tevatron should be more promising as a test of non-DGLAP dynamics compared to HERA due to higher energy and therefore a larger phase space open to gluon emissions. While at HERA, the separation between the struck quark and forward jet can reach up to about four units of rapidity, the measurable jet separation at the Tevatron is up to six units. Although

the BFKL calculations are expected to be more reliable at high energies, it should be kept in mind that energy-momentum conservation is not fulfilled. Thus, effects due to the conservation of energy and momentum (consistency constraint) will be significant.

In Table 1 we present a collection of various experimental results from HERA and the Tevatron which relate to low x physics and we state the result of the comparison of these data with NLO DGLAP theory and BFKL and/or CCFM evolution schemes. The aim of this section is to review some of the items in Table 1 in more detail. In the next two subsections we review measurements which can be well described by the DGLAP approximation and then discuss measurements which were especially designed to extract a BFKL signal i.e. where the DGLAP evolution was suppressed by experimental cuts.

4.1 Where NLO DGLAP (almost) works

Several programs exist for the numerical NLO calculation of jet observables at the parton level in collinear factorization. They are known to give comparable results. All of them calculate the direct photon contributions to the cross sections. Only the JetVip program [180, 181] provides the additional possibility to calculate a cross section consisting of both direct and resolved photon contributions; however, in the DIS case conceptual difficulties are encountered [182] which lead to ambiguous results.

All the parton level calculations in the collinear approach presented in this paper were performed using the DISENT program [183] and the CTEQ6M [184] set of parton distribution functions. The renormalization scale was set to $\mu_{\text{r}} = \sum p_{\perp i}$ and the factorization scale $\mu_{\text{f}} = Q$.[11]

There has been some confusion in the literature concerning the concept of NLO. Formally, whether a calculation is leading or next-to-leading depends on the observable. LO is then the lowest order in α_{S} in which the observable obtains a non-zero value, and NLO is one order higher in α_{s}. However, sometimes it is difficult to define the order in α_{s} appropriate for a specific measurement. Therefore, in this paper we state clearly to which order in α_{s} a process has been calculated. In Fig. 17 representative diagrams are shown for NLO calculations of single-jet (F_2), dijet and 3-jet processes. It is obvious from Fig. 17 that NLO dijet calculations do not include all diagrams necessary for a NNLO single-jet calculation, as indicated in the right column of Fig. 17.

The calculations summarized above use integrated parton distributions, convoluted with LO or NLO coefficient functions. As is usual in the standard formulation of factorization, the coefficient functions are on-shell partonic cross sections with subtractions of the singular collinear regions. The parton distributions are typically in the $\overline{\text{MS}}$ scheme, where the partons are integrated over *all* transverse momentum with the resulting ultra-violet divergences being canceled by renormalization in the $\overline{\text{MS}}$ scheme. There is an

---

[10] The pseudorapidity η_{lab} is defined as $\eta_{\text{lab}} = -\ln\tan(\theta/2)$, with polar angle θ being measured with respect to positive z-axis, which is given by the proton beam (or forward) direction

[11] For technical reasons DISENT allows only $\mu_{\text{f}} = Q$ or $\mu_{\text{f}} = $ const.

Table 1. Summary of the ability of the collinear and $k_\perp$-factorization approaches to reproduce the current measurements of some observables: *ok* means a satisfactory description; 1/2 means not a perfect but also not too bad a description, or in part of the phase space an acceptable description; *no* means that the description is bad; and ? means that no thorough comparison has been made. The label *NLO dijet* means that the calculation was performed in next-to-leading order for a dijet configuration available for example in the DISENT, MEPJET or DISASTER++ programs. LO + PS is short for LO matrix element + parton shower calculations as implemented in LEPTO [174] or RAPGAP [175] in the collinear approach and LDC [2–5] or CASCADE [6,7] in the $k_\perp$-factorization approach

	Collinear factorization				$k_\perp-$
	direct			resolved	factorization
	LO + PS	higher order NLO (dijet)	LO + PS	higher order NLO (dijet)	LO + PS
HERA observables					
DIS D^* production		ok [122, 123]	?	?	ok [123, 124]
photoprod. of D^*	ok	ok [125, 126]	ok [125]	no [125]	ok [6, 124, 127–129]
DIS B production (visible)	ok [130]	ok [130]	–	–	ok [130]
DIS B production (total)	no [131]	ok [131]	–	–	no [131]
photoprod. of B (visible)	ok [132, 133]	?			ok [134, 135]
photoprod. of B (total)	no [133, 136]	no [126, 133, 136]	?	?	ok [134, 135]
high Q^2 dijets	?	ok [137, 138]	?	?	?
low Q^2 dijets (cross sec.)	? ?	ok [139]	?	no [137, 138, 140]	?
low Q^2 dijets (azim.corr.)	no [139]	no [139] NLO 3-jet no [139]	ok [139]	?	ok [139]
photoprod. of dijets	?	ok [141]	?	no [140, 142] ok [141]	?
particle spectra	no [143, 144]	–	ok [145]	–	ok [6]
energy flow	no [143, 146, 147]	–	ok [145, 147]	–	?
HERA small-x observables					
DIS forward jet production	no [148–152]	no [151–153]	ok [149–152, 154]	ok [152, 153]	ok [6]
DIS forward π production	no [155, 156]	?	ok [155, 156]	?	1/2 [156]
DIS J/ψ prod.	?		?	?	ok [118, 157]
photoprod. of J/ψ	no [158]	ok [159]		ok [160]	ok [118, 161, 162]
J/ψ polarization				low.stat. [160]	low.stat. [118, 163]
Tevatron observables	direct		heavy quark excitation		
D meson prod.			no	?	ok [164, 165]
J/ψ prod.	ok [100, 102, 103, 166, 167]				ok [113, 114, 117]
χ_c prod.	ok [102, 103]				ok [116, 117]
J/ψ polarization	low.stat. [168]	no	no	no	ok [114, 117]
high-$p_\perp$ B prod.	no [169]	ok [170]	ok [169]	?	ok [135, 164, 171–173]
$b\bar{b}$ (azim.corr.)		ok [170]			ok [173]
Υ prod.	ok [102, 103]				ok [117]
high-$p_\perp$ jets at large $|\Delta\eta^\star|$	no	?		?	?

evident mismatch of approximated and exact parton kinematics in such calculations. For the infra-red-safe jet cross sections that are the domain of validity of the calculations, the factorization theorem ensures that the calculations are consistent and valid.

The transverse momenta of the partons entering the hard scattering can be seen as being generated by two sources: the intrinsic (primordial) transverse momentum, which reflects the Fermi motion of the partons in the hadron, typically of the order of 1 GeV, and the transverse momentum generated by the QCD evolution (DGLAP or BFKL/CCFM/LDC), which can reach large values, even in DGLAP up to the factorization scale. Therefore, for more exclusive components of the cross section, it is better to use suitably defined unintegrated distributions and off-shell parton kinematics. For one treatment along these
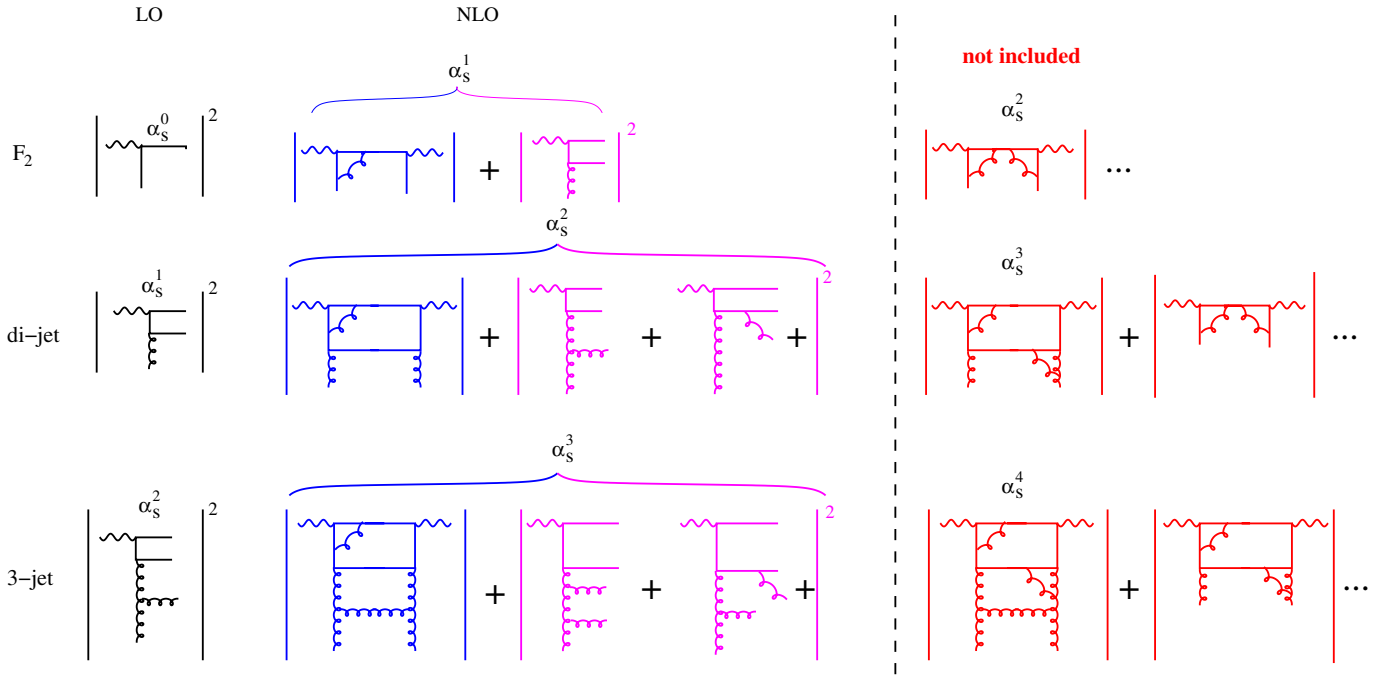
Fig. 17. Schematic picture of the diagrams which are included in NLO calculations for single-jet (F_2), dijet and 3-jet processes. Also indicated are example of diagrams which are not included (since of higher order in α_s or not contributing to the n-jet observable)

lines that is specifically designed to treat NLO corrections in the context of showering Monte Carlo event generators, see the paper of Collins and Zu [185].

4.1.1 The longitudinal structure function $F_L(x, Q^2)$

The longitudinal structure function $F_L(x, Q^2)$ is dominated by the gluon density at large enough Q^2. In the limit of small Q^2 there is no phase space for strong ordering in virtuality (DGLAP will not work) and unphysically negative values for $F_L(x, Q^2)$ are obtained in some calculations for $Q^2 < 1\,\mathrm{GeV}^2$ [186]. However, in the $k_\perp$-factorization approach there is no strong ordering in virtuality and therefore the parton evolution may generate arbitrarily small $k_\perp$ (down to an artificial cutoff) which means that the parameterization is valid over the full range in $k_\perp$. In Fig. 18 the structure function $F_L(x, Q^2)$ as measured by H1 and ZEUS [187] is compared to calculations using $k_\perp$-factorization in the framework of [188]. The unintegrated gluon density was taken from CCFM (J2003 set 1). Shown for comparison is another unintegrated gluon density obtained from the derivative of the integrated gluon density (here GRV [99] is used) and the prediction for F_L obtained in the collinear DGLAP approach using the MRST2002 [189] parton densities.

4.1.2 Single inclusive jets at HERA

Jets have been studied extensively at HERA and other colliders. These measurements have shown that at sufficiently
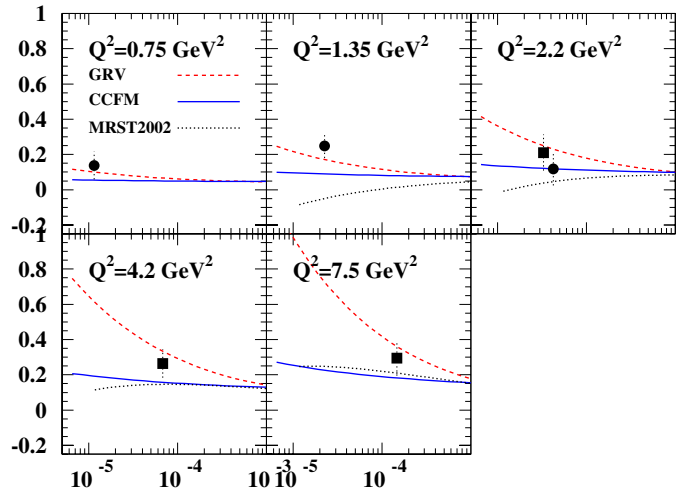

Fig. 18. The longitudinal structure function $F_L(x, Q^2)$ as measured by H1 and ZEUS [187] compared to different calculations, including also the collinear DGLAP approach

large transverse momenta and/or momentum transfers the NLO QCD theory based on the DGLAP approximation is in excellent agreement with the data. To judge how well this approximation works let us mention that the determination of the strong coupling constant α_s from recent H1 [190] and ZEUS [191] jet measurements are not only in perfect agreement with the world average value but are also in precision comparable to LEP measurements. Another example of a jet measurement fully compatible with NLO theory in the collinear approach is the measurement of dijet angular distributions [192] performed by the D0 Collaboration.
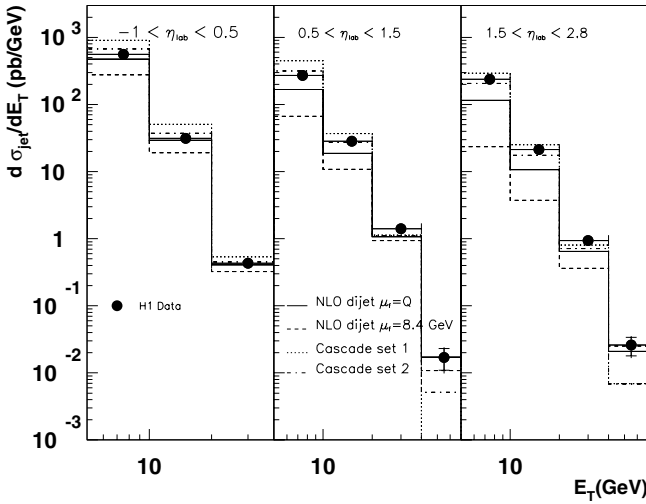
Fig. 19. Inclusive jet cross section $\mathrm{d}\sigma_{\mathrm{T,jet}}/\mathrm{d}E_{\mathrm{T}}$ in different ranges of η_{lab}, integrated over the region $5 < Q^2 < 100\,\mathrm{GeV}^2$ and $0.2 < y < 0.6$. The data are compared to NLO dijet calculation (DISENT) and to the predictions from CASCADE

The result of the data–theory comparison is an exclusion limit on the quark substructure which is competitive with many LEP results. In spite of this spectacular success of the QCD theory in the collinear approach one should keep in mind that there are regions of phase space, where the description of the data is less than satisfactory. It is the aim of this subsection to localize these regions and observe patterns characteristic for a possible failure to describe the data by NLO theory in the collinear approximation.

In a recent H1 paper [193], NLO calculations of the inclusive jet cross sections, using the DISENT program [183], were confronted with high statistics data. The kinematic range considered in this analysis was constrained by the conditions $5 < Q^2 < 100\,\mathrm{GeV}^2$ and $0.2 < y < 0.6$ (the latter condition leads to a reduction of photoproduction

background). Jets are defined using the inclusive $k_\perp$-cluster algorithm [194, 195] in the Breit frame[12] and selected by the requirement $E_{\mathrm{T,jet}} > 5\,\mathrm{GeV}$.

Figure 19 shows the inclusive jet cross section as a function of the transverse jet energy $E_{\mathrm{T,jet}}$ in different regions of the pseudorapidity η_{lab}: in the backward region $-1 < \eta_{\mathrm{lab}} < 0.5$, the central region $0.5 < \eta_{\mathrm{lab}} < 1.5$ and the forward region $1.5 < \eta_{\mathrm{lab}} < 2.8$. The measured cross sections, which extend over four orders of magnitude, are compared to the calculations obtained in the collinear and $k_\perp$-factorization approaches, respectively.

While there is good agreement between the data and the NLO dijet calculation in the backward region for all $E_{\mathrm{T,jet}}$ values, discrepancies are observed for more forward jets with low $E_{\mathrm{T,jet}}$. In the lowest $E_{\mathrm{T,jet}}$ range ($5 < E_{\mathrm{T,jet}} < 20\,\mathrm{GeV}$, for $\eta_{\mathrm{lab}} > 1.5$), the assumed renormalization scale uncertainty ($E_{\mathrm{T,jet}}/2 < \mu_{\mathrm{r}} < 2E_{\mathrm{T,jet}}$) does not cover the large difference between the data and the calculation. In Fig. 20 the forward region from Fig. 19 is studied in bins of Q^2, showing that discrepancies to NLO dijet calculations are most significant at small Q^2 and small $E_{\mathrm{T,jet}}$ values. The factorization scale uncertainty is estimated by changing $\mu_{\mathrm{f}} = \sqrt{Q^2}$ to $\mu_{\mathrm{f}} = 8.4\,\mathrm{GeV}$, which is the average jet transverse momentum. The correlation of large NLO/LO corrections and high sensitivity to renormalization scale variations with poor agreement between data and QCD predictions strongly suggests that the inclusion of higher order (e.g. NNLO or resolved photon component) terms in the QCD calculations is necessary in order to improve the description of the data.

The predictions obtained in the $k_\perp$-factorization approach, supplemented with the CCFM unintegrated gluon densities, as implemented in CASCADE, are in reasonable

---

[12] The Breit frame is defined by $2x\mathbf{p} + \mathbf{q} = 0$, where x is the Bjorken scaling variable, and $\mathbf{p}$ and $\mathbf{q}$ are the proton and the virtual photon momenta, respectively.
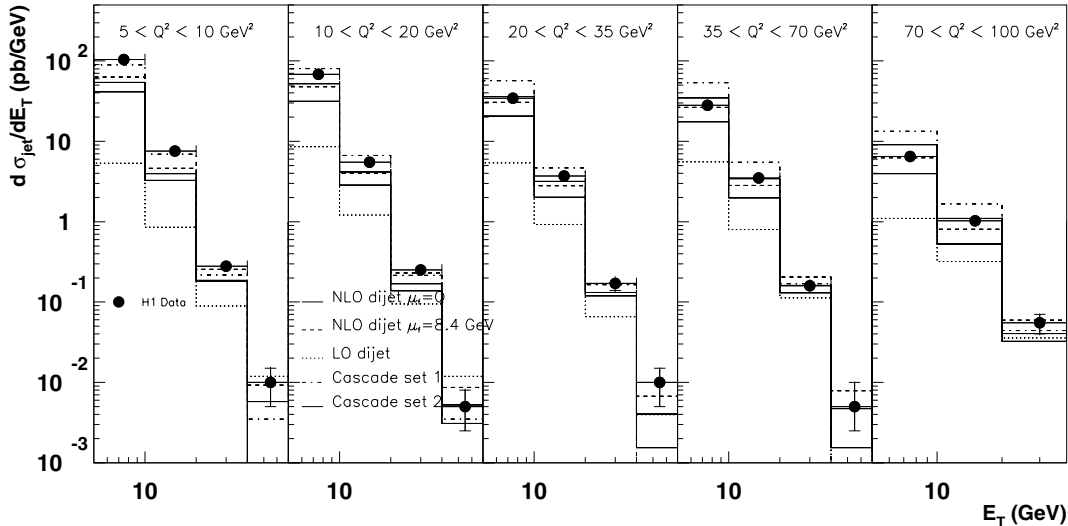

Fig. 20. Inclusive jet cross section $\mathrm{d}\sigma_{\mathrm{Jet}}/\mathrm{d}E_{\mathrm{T}}$ for the forward region $1.5 < \eta_{\mathrm{lab}} < 2.8$ in different ranges of Q^2. The NLO dijet (DISENT) and the LO dijet calculation as well as the prediction CASCADE are shown

agreement with the data. Especially the forward region (Fig. 20) is reasonably well described. The quality of the various approaches to describe the data can be seen in Table 2, where we quote the $\chi^2/$ndf, both for the NLO dijet and the CASCADE calculations.

It is interesting to quote in the above context the recent ZEUS measurement on inclusive jets [197] presented in Fig. 21. The cross section for jets reconstructed in the laboratory frame with the inclusive $k_\perp$ algorithm is compared to a calculation in NLO (here $\mathcal{O}(\alpha_s)$). When going from small towards large values of $\eta_{\rm jet}$ the description of the data by the NLO calculation becomes worse. The reason for this is that the α_s^0 contribution goes to zero and the $\mathcal{O}(\alpha_s)$ calculation becomes essentially the LO contribution, since for a fixed Q^2 and x (or y), $\eta_{\rm jet}$ is fixed in an α_s^0 calculation, simply given by $\frac{1}{2}\ln\frac{Q^2(1-y)}{4E_e^2y^2}$. The range used in the measurement is $Q^2 > 25\,\mathrm{GeV}^2$, $y > 0.04$ which, for the lowest Q^2 gives a maximum $\eta_{\rm jet}$ of about 0.8. For larger Q^2 the maximum $\eta_{\rm jet}$ is a bit larger, but the suppression of the α_s^0 contribution is still visible in Fig. 21 around $\eta_{\rm jet} = 1$. Beyond this, the lowest order contribution is dominated by α_s^1 and the "NLO" calculation in the figure becomes leading order. As can be seen from Fig. 21, even DGLAP type Monte Carlo models (here LEPTO) give a rather reasonable description, if further parton radiation is included via parton showers. Thus this comparison shows the need for higher order corrections but not necessarily a need for any BFKL contribution.
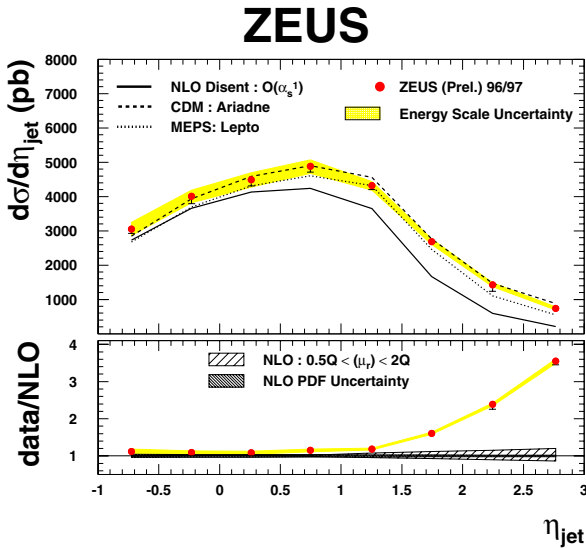
4.1.3 Inclusive dijets at HERA

The measurement of dijet production, which is less inclusive compared to the measurement described before, might provide a stronger test of the NLO QCD calculations in the collinear factorization approach, as it involves more observables. Experimentally, possible deviations from the DGLAP approach can best be observed by selecting events in a phase space regime, where the main assumption, the strong ordering in $k_\perp$ of the exchanged parton cascade (Fig. 22), is no longer strictly fulfilled. This is the case at small x. The parton configurations not included in DGLAP based calculations might contribute significantly to the cross section. Moreover, with respect to the photon–proton center of mass system (hcms), the two partons produced in a hard scattering process (Fig. 22) are no longer balanced in transverse momentum. Events coming from calculations beyond $\mathcal{O}(\alpha_s)$ will lead to a situation where the two hard jets are no longer back-to-back. The excess of such events is expected to be higher for a BFKL scenario compared to DGLAP, due to the possibility of hard emissions in the parton evolution provided by the non-ordering in $k_\perp$.

Dijet production in deep inelastic ep scattering was investigated in the region of low x $(10^{-4} < x < 10^{-2})$ and low Q^2 $(5 < Q^2 < 100\,\mathrm{GeV}^2)$ [139]. Jets were reconstructed in the hcms using the $k_\perp$ algorithm. A minimum transverse jet energy $E_T^\star$ of 5 GeV was required and an additional requirement on the most energetic jet $E_{T,\rm max}^\star > 7\,\mathrm{GeV}$ (in the hcms) was added to avoid a scenario for which NLO dijet predictions become unreliable [198,199]. In Fig. 23 the triple differential inclusive dijet cross section in bins of Bjorken variable x and Q^2 as a function of the distance $|\Delta\eta^*|$ between the jets is presented. The data are compared to NLO dijet predictions. The NLO dijet calculation with $\mu_{\rm f}^2 = Q^2$ falls well below the data. A better description over the full phase, including the regime of very low x, is obtained using $\mu_{\rm f}^2 = 70\,\mathrm{GeV}^2$. It should be noted however, that even with $\mu_{\rm f}^2 = 70\,\mathrm{GeV}^2$ the theoretical uncertainty due to scale dependence of the NLO calculation is rather large so again no strong statement about the DGLAP approximation for dijet production at low x can be made on the basis of the cross section measurement alone. In Fig. 23 the data are also compared with the predictions using the $k_\perp$-factorization approach in CASCADE. The quality of the data description is again quoted as $\chi^2/$ndf for both approaches in Table 2.

Further insight into small-x dynamics may be gained from inclusive dijet data by studying the behavior of events with a small separation in the azimuthal angle, $\Delta\phi^*$, of the two hardest jets as measured in the hcms, as proposed in [200–203]. Partons entering the hard scattering process with negligible transverse momenta, as assumed in the DGLAP formalism, lead mainly to back-to-back configurations of the two outgoing jets with $\Delta\phi^* = \pi$. Higher order QCD processes lead to azimuthal jet separations different from π; however, the effect might be smaller than in the case of the BFKL and CCFM evolution schemes. In the above quoted dijet analysis [139] the jet azimuthal de-correlation was studied using a variable which has been proposed by Szczurek et al. [203]:

Fig. 21. Upper part: Measured differential inclusive jet cross section $\mathrm{d}\sigma/\mathrm{d}\eta_{\rm jet}$ for the inclusive phase space compared to ARIADNE (CDM), LEPTO (MEPS) and NLO Disent in order $\mathcal{O}(\alpha_s^1)$ Lower part: Relative difference of the measured inclusive jet cross section $\mathrm{d}\sigma/\mathrm{d}\eta_{\rm jet}$ to the NLO DISENT calculation with renormalization scale $\mu_{\rm r}^2 = Q^2$

Table 2. Comparison of χ^2/ndf obtained from comparing different predictions to the data. For the NLO dijet calculation with the DISENT program the renormalization scale was set to $\mu_\mathrm{r} = \sum k_\perp$, the CTEQ6M [184] and SaS [196] parton distribution functions of the proton and photon, respectively, are used

	NLO dijet		CASCADE J2003		RAPGAP dir	RAPGAP dir + res	
parton density	CTEQ6M	CTEQ6M	set 1	set2	CTEQ6M	CTEQ6M + SaS	
factorization scale μ_f^2	70 GeV^2	Q^2				$Q^2 + p_\perp^2$	$Q^2 + 4p_\perp^2$
$\mathrm{d}\sigma/\mathrm{d}E_t$ (in bins of η) (cf. Fig. 19)	12.8	13.2	25.5	4.0	23.7	1.3	8.6
$\mathrm{d}\sigma/\mathrm{d}E_t$ (in bins of Q^2 for $1.5 < \eta < 2.8$) (cf. Fig. 20)	3.9	13.6	17.3	6.0	13.2	2.1	13.2
$\mathrm{d}\sigma/\mathrm{d}\Delta\eta$ (cf. Fig. 23)	40.1	40.9	116.8	37.7	66.9	22.6	46.7
$S = \frac{\int^\alpha N_{2-\mathrm{jet}}(\Delta\phi^*, x, Q^2)\mathrm{d}\Delta\phi^*}{\int N_{2-\mathrm{jet}}(\Delta\phi^*, x, Q^2)\mathrm{d}\Delta\phi^*}$ (cf. Fig. 24)	17.8	15.7	23.2	3.9	3.3	2.6	1.7
forward jets H1 $p_\perp > 3.5$ GeV (cf. Fig. 25(a))	8.9	17.0	2.7	4.7	10.8	4.4	0.3
forward jets H1 $p_\perp > 5$ GeV (cf. Fig. 25(b))	5.7	11.2	1.9	2.3	6.7	2.6	0.7
forward jets H1 prel $p_\perp > 3.5$ GeV (cf. Fig. 26)	1.7	6.4	1.3	1.1	4.4	0.9	1.7
forward jets ZEUS $p_\perp > 5$ GeV (cf. Fig. 27)	28.9	38.4	19.2	9.5	27.1	20.1	16.8

$$S = \frac{\int_0^\alpha N_{2-\mathrm{jet}}(\Delta\phi^*, x, Q^2)\mathrm{d}\Delta\phi^*}{\int_0^{180^\circ} N_{2-\mathrm{jet}}(\Delta\phi^*, x, Q^2)\mathrm{d}\Delta\phi^*}, \ 0 < \alpha < 180^\circ, \quad (33)$$

with α being a parameter for the $\Delta\phi^*$ distribution. Its advantage in comparison with the direct $\Delta\phi^*$ measurement (see e.g. the analysis of the Tevatron data, Sect. 4.2.3) is its better stability against migrations. For the data presented in Fig. 24 $\alpha = 120^\circ$ was chosen. This choice is mainly dictated by the limited jet energy resolution which may result in an incorrect choice of the two most energetic jets. Figure 24 presents the S distribution as a function of x in bins of Q^2. The measured value of S is of the order of 5% and increases with decreasing x. This rise is most prominent in the lowest Q^2 bin. On the contrary, the NLO dijet QCD calculation predicts S values of order 1%, several standard deviations below the data, and show no rise toward small x. Here the NLO calculations are performed in the on-shell limit (see discussion in Sect. 4.1), neglecting the transverse momentum coming from the QCD evolution. Therefore only the $\mathcal{O}(\alpha_\mathrm{s}^2)$ part of the matrix elements gives a significant contribution for $\Delta\phi^* \neq 180^\circ$. The calculation of NLO 3-jet is in much better agreement with the data (shown in [139]) which is NLO for the S variable, but it still fails to describe the rise towards small x. Since Monte Carlo generators, like RAPGAP, include the effects of the finite transverse momentum of the incoming partons via parton showers, it is not surprising, that they come much closer to the data than the naive NLO calculation ignoring the off-shellness of the incoming partons. This shows that care has to be taken by applying fixed-order partonic calculations to exclusive observables.

The CCFM evolution as implemented in CASCADE [41] describes the data reasonably well (Fig. 24), but this is also true if a resolved component of the virtual photon is added, provided that a rather large scale $\mu_\mathrm{r}^2 = Q^2 + 4p_\perp^2$ is chosen (to get a large enough resolved contribution).

To conclude this section let us summarize its main points.
(1) For the inclusive jet cross section in DIS, the NLO dijet description starts to fail when jets become more and more forward.
(2) The worsening of the description is accompanied by increasing theoretical uncertainty due to scale dependence, indicating that the NNLO terms may be more important in the forward direction.
(3) NLO dijet calculations describe dijet cross section in DIS data very well, down to $x_\mathrm{Bj} = 10^{-4}$ in the central region of rapidity, if $\mu_\mathrm{f}^2 = 70$ GeV^2 is used. For $\mu_\mathrm{f}^2 = Q^2$ the description is much worse.
(4) The largest differences between NLO theory for the inclusive jet and dijet cross section and the data are observed in the small-x, small-Q^2 region.
(5) The azimuthal jet de-correlation in dijet DIS data is not described by NLO dijet calculation, which is effectively LO for that observable. The NLO 3-jet calculation is in better agreement with the data but still at small x is not sufficient. The CCFM evolution approach is consistent with the data, but so is the LO ME + DGLAP parton shower approach provided that the resolved photon contribution is taken into account with a scale given by $Q^2 + 4p_\perp^2$.
(6) As in the case of cross sections, the largest discrepancies for azimuthal de-correlation are found in the small-x, small-Q^2 region.

4.2 Where NLO DGLAP does not work

4.2.1 Forward jets in DIS

Measurements described as "Mueller forward jets in DIS" [177–179] were especially designed to search for non-DGLAP evolution signatures. The following conditions were required to suppress the DGLAP and enhance the BFKL evolution (with $x_\mathrm{jet} = E_\mathrm{jet}/E_p$).
(1) A high energetic jet with an energy fraction $x_\mathrm{jet} \gg x_\mathrm{Bj}$ to enhance BFKL x-space evolution.
(2) A high enough transverse momentum $E_\mathrm{T,jet}$ of the jet to ensure that perturbative calculations are valid e.g. $E_\mathrm{T,jet} > 3.5$ GeV.
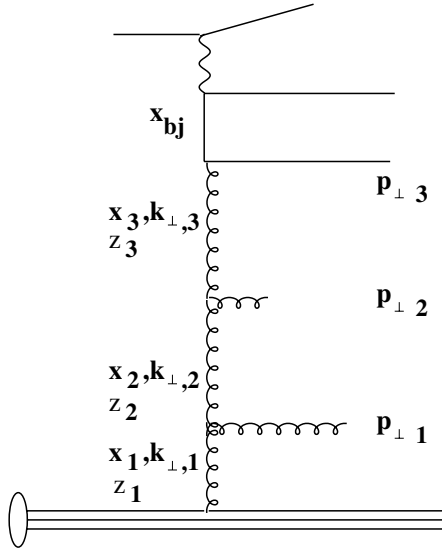(3) $E_\mathrm{T,jet} \approx Q$ in order to suppress the DGLAP evolution.

Fig. 22. Generic leading order diagrams for dijet production in ep scattering: the variables $k_{\perp i}$, x_i and z_i denote the transverse momenta, the longitudinal energy fractions and the fractional energy in the splitting, respectively, and $p_{\perp i}$ are the transverse momenta of the radiated gluons
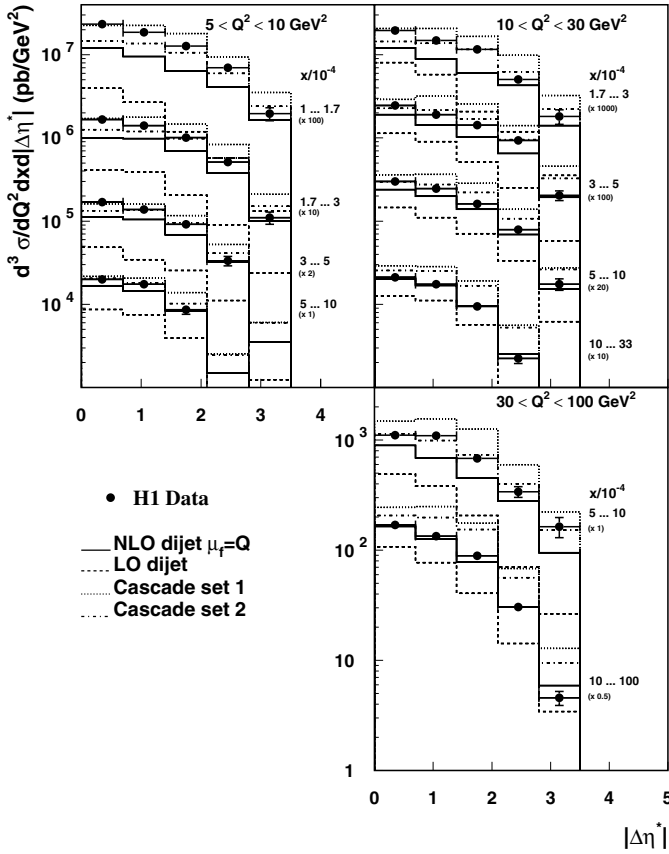

Fig. 23. The triple differential inclusive dijet cross section in bins of the Bjorken variable x and Q^2 as a function of the distance $|\Delta\eta^*|$ between the dijets compared to NLO dijet calculation (DISENT, solid line) and predictions from Cascade(dashed and dotted line)
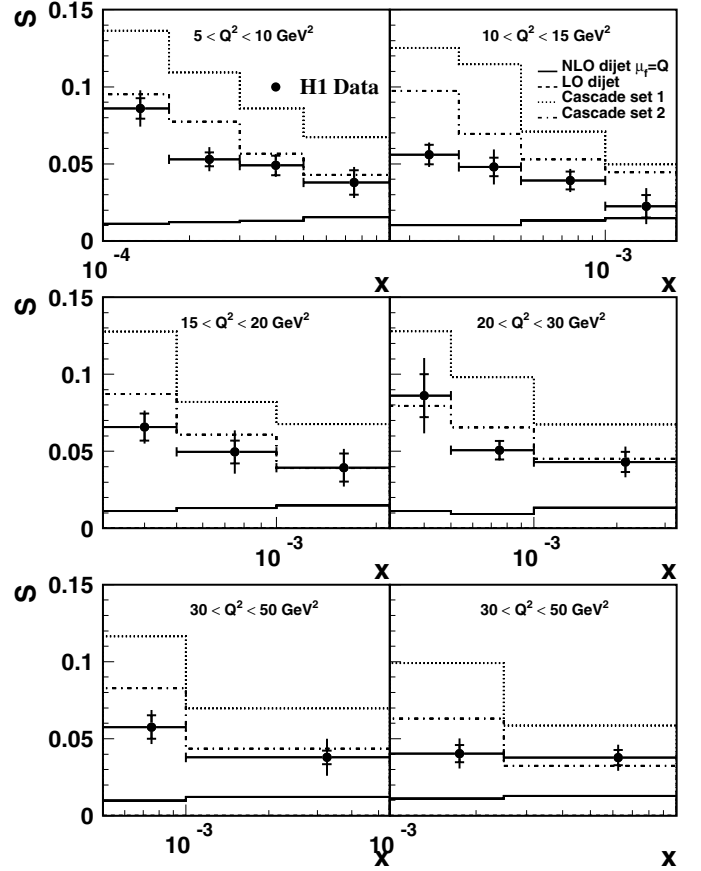
Fig. 24. Ratio S of the number of events with a small azimuthal jet separation ($\alpha < 120^\circ$) of the two most energetic jets with respect to the total number of inclusive dijet events, given as a function of the Bjorken variable x and Q^2. The data are compared to NLO dijet calculations (DISENT, solid line) and predictions from Cascade

At HERA, the requirement of $x_{\text{jet}}/x_{\text{Bj}}$ to be large results in typical jet angles of a few degrees with respect to the forward (proton) direction. Due to the unavoidable beam-pipe hole in the detector, the acceptance is limited to jets with an angle larger than, for example, 7° in the H1 detector. At smaller angles the jets are insufficiently contained in the detector and the experimental separation from proton remnant fragments might be difficult. As the jet approaches more and more the forward direction its profile gets thicker and more asymmetric and a large fraction disappears down the beam hole. In fact, the observation of broadening of the jet profile leads the ZEUS collaboration to restrict the forward jet analysis to pseudorapidities $\eta_{\text{jet}} < 2.6$ corresponding to the limiting angle $\Theta_{\text{jet}} > 8.5^\circ$. The criterion which determines the minimum acceptable jet angle is a satisfactory description of the jet profile. Obviously, the jet profile and separation of the remnant fragmentation depends on the jet algorithm. In the ZEUS analysis [150] the cone algorithm was employed. In principle an algorithm like the $k_\perp$-cluster algorithm, which is not based on geometry, should be less sensitive to detector

Table 3. Summary of the different selection criteria used to define *Mueller forward jets* in the H1 [151] and ZEUS [150] measurements

	H1 cuts	ZEUS cuts
E'_e	$> 11\,\mathrm{GeV}$	$> 10\,\mathrm{GeV}$
y_e	> 0.1	> 0.1
$E_{\mathrm{T,jet}}$	$> 3.5\ (5)\,\mathrm{GeV}$	$> 5\,\mathrm{GeV}$
η_{jet}	1.7–2.8	< 2.6
$E_{\mathrm{T,jet}}/Q^2$	0.5–2	0.5–2
x_{jet}	> 0.035	> 0.036
$p_{z,\mathrm{jet}}^{\mathrm{Breit}}$		> 0
x	0.0001–0.004	0.00045–0.045

edges, and the separation of remnant fragments should be easier in the Breit frame.

The condition $E_{\mathrm{T,jet}}^2/Q^2 \approx 1$ is essential to suppress the DGLAP evolution in direct photon interactions. Due to limited statistics a compromise has to be found. In practice an interval is defined around this central value of $E_{\mathrm{T,jet}}^2/Q^2$. The requirement $E_{\mathrm{T,jet}} \approx Q$ leads to another experimental challenge: to reconstruct jets of the smallest possibly transverse momentum, forward jets at smallest possibly Q^2 (but still in perturbative region) and hence smallest possible x are required.

It should be noted that at HERA energies the above cuts restrict the phase space not only for DGLAP but for any type of evolution. At HERA the range between the hard scattering and the forward jet covers about 4 rapidity units, limiting the number of hard emissions to about 3–4. Therefore, it may be that there is not enough phase space for a BFKL–DGLAP discrimination. In Fig. 16 (right) a typical Feynman diagram for forward jets and particles is shown.

In Table 3 we present cuts used in the H1 [151] and ZEUS [150] forward jet analyses, performed with the cone algorithm. In spite of small differences of the selected phase space, it is clear that cross sections at $E_{\mathrm{T,jet}} > 5\,\mathrm{GeV}$ are compatible (see Figs. 25b and 27). Recently the H1 Collaboration performed a new measurement of the forward jet cross section [149] using much higher statistics and applying cuts almost identical to those applied in [151] ($5 < Q^2 < 75\,\mathrm{GeV}^2$, $E_{\mathrm{T,jet}} > 3.5\,\mathrm{GeV}$, $7° < \theta_{\mathrm{jet}} < 20°$, $x_{\mathrm{jet}} = E_{\mathrm{jet}}/E_p > 0.035$, $0.5 < E_{\mathrm{T,jet}}^2/Q^2 < 2$). In this analysis the jets were reconstructed using the inclusive $k_\perp$ algorithm. The cross section for forward jet production [149, 151] as a function of x is shown in Figs. 25, 26 and 27. The measurements are up to a factor of two larger than the prediction based on $\mathcal{O}(\alpha_s)$ (and also $\mathcal{O}(\alpha_s^2)$) QCD calculations in the DGLAP approach. Such parton level calculations are compared in Figs. 25, 26 and 27 with the measurement. Also shown is a comparison with different unintegrated gluon densities implemented in CASCADE [6, 7], which shows the sensitivity of the predicted forward jet cross section on the details of the unintegrated gluon density. It is interesting to note that also including the nonsingular terms in the CCFM splitting function (J2003 set 2) leads to reasonable agreement with the measurements in
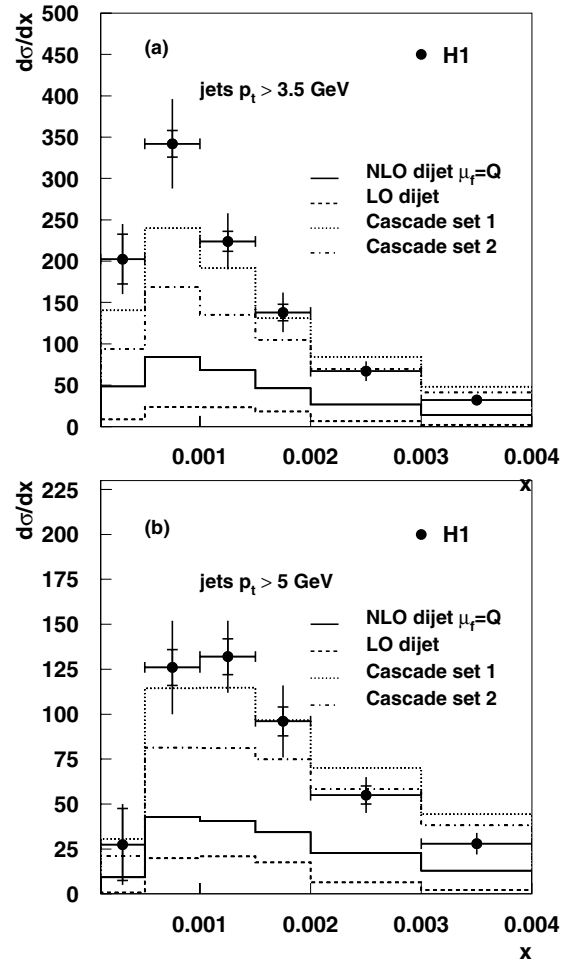

Fig. 25. The cross section for forward jet production [151] at the hadron level, as a function of x for **a** $E_{\mathrm{T,jet}} > 3.5\,\mathrm{GeV}$ and **b** $E_{\mathrm{T,jet}} > 5\,\mathrm{GeV}$. Also shown are the predictions from LO and NLO dijet calculations as well as predictions from CASCADE
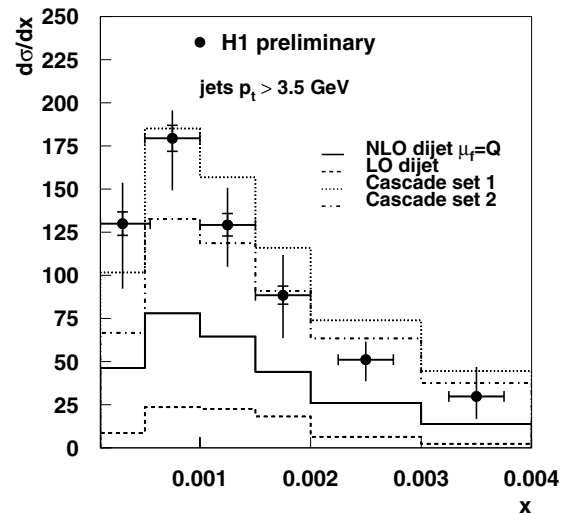

Fig. 26. The cross section for forward jet production [149] at the hadron level, as a function of x for $E_{\mathrm{T,jet}} > 3.5\,\mathrm{GeV}$. Also shown are the predictions from LO and NLO dijet calculations as well as predictions from CASCADE
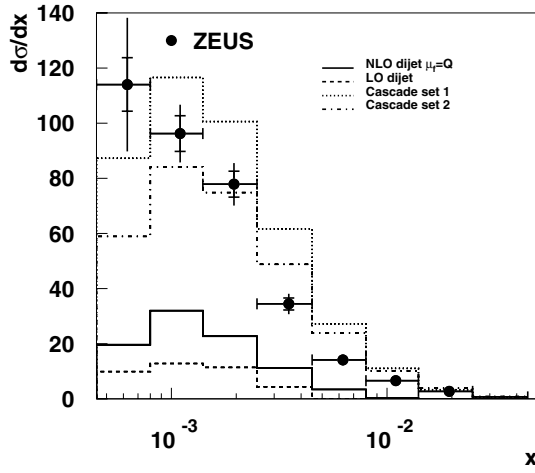
Fig. 27. Forward jet cross section [150] as a function of x in the kinematic region given in Table 2. Shown are LO and NLO dijet calculations together with predictions from CASCADE

Figs. 26 and 27. For all other distributions, e.g. $d\sigma/dp_{\perp \text{ jet}}$, the pattern of agreement/disagreement is similar. The level of agreement with the measured cross section of forward jet production is given in Table 2.

The forward jet cross section was also studied using the BFKL formalism [12–14]. In particular Kwieciński, Martin and Outhwaite (KMO) in [204] used a modified LO BFKL equation, supplemented by a consistency constraint which mimics higher orders of the perturbative expansion, to describe the inclusive forward jet cross section. The KMO
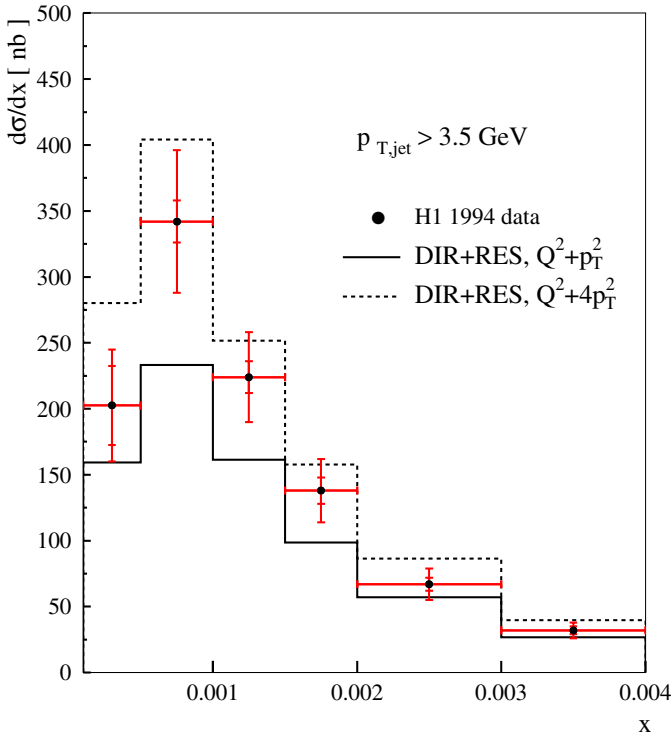

Fig. 28. The predictions of the RAPGAP Monte Carlo (dir + res) at two different scales compared to the data of [151] (cone jet algorithm)
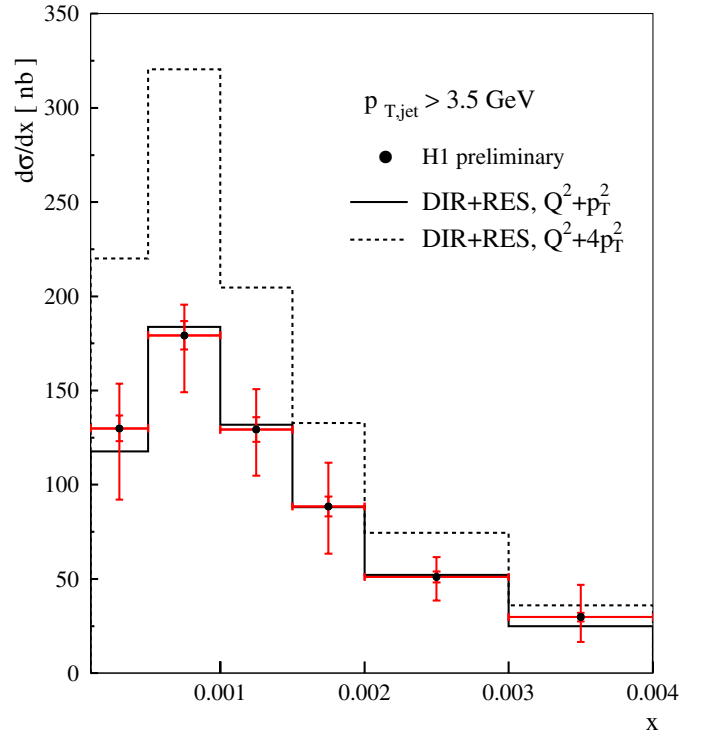

Fig. 29. The predictions of the RAPGAP Monte Carlo (dir + res) at two different scales compared to the data of [149] ($k_\perp$ jet algorithm)

model describes the data well, however the predicted cross section is very sensitive to the input parameters in particular to the infrared cutoff and the scale of α_s. Thus the model has rather large uncertainties in the normalization of the cross section, whereas the shape of the distribution in Bjorken variable x is expected to be more stable. We will come back to the KMO calculation in the next section.

The choice of the jet algorithm has quite an effect on the measured cross section, as we can see comparing Fig. 29 (data from [149], $k_\perp$ jet algorithm in a Breit frame) and Fig. 28 (data from [148], cone jet algorithm in a laboratory frame). The cross sections come out different at hadron level due to the choice of the jet algorithm.

Including a contribution from resolved virtual photons (as done in RAPGAP RES [175]) (we abbreviate "resolved" by RES, and "direct" by DIR) leads also to a reasonable description of the forward jet data. It should be noted however, that the predictions of the model are sensitive to the renormalization and factorization scales. The RAP-GAP package allows a choice of renormalization and factorization scale, and in Figs. 28 and 29 the predictions are presented for two different choices, $\mu^2 = Q^2 + p_\perp{}^2$ and $\mu^2 = Q^2 + 4p_\perp{}^2$, where $p_\perp$ is the transverse momentum of the partons taking part in the hard scattering process. The errors (mainly systematic) are large and reasonable agreement with the data would still be achieved for a scale of $Q^2 + 4p_\perp{}^2$. Note, that for a correct description of the azimuthal de-correlation by RAPGAP the same large scale has to be employed (see Sect. 4.2.2). However it seems that the two different forward jet measurements prefer different

choices of the scales: in Fig. 29 the forward jet data are well described with a renormalization scale $\mu_r^2 = Q^2 + p_\perp{}^2$ while the forward jet data of Fig. 28 lie between the predictions using $\mu_r^2 = Q^2 + p_\perp{}^2$ and $\mu_r^2 = Q^2 + 4p_\perp{}^2$. Both calculations use RAPGAP and the same (CTEQ6M and SaS1d) proton and photon PDF's.

Before coming to the end of this subsection, let us comment on possibilities of a new type forward jets measurements, which open with the advent of high statistics data. Obviously we can go to higher Q^2 and higher $x_{\rm jet}$ so that the ratio $x_{\rm jet}/x_{\rm Bj}$ would remain large. An example of such a scenario is $Q^2 > 16\,{\rm GeV}^2, p_{\perp\,\rm jet} > 6\,{\rm GeV}, x_{\rm jet} > 0.05, 0.1 < y < 0.7$. The cross section calculated using RAPGAP and CASCADE is shown in Fig. 30. It is 3–5 times lower than measurement with cuts presented in Table 3, but is certainly measurable at the level of $100\,{\rm pb}^{-1}$ and has several advantages. The jets with higher $p_\perp$ and higher $x_{\rm jet}$ are cleaner, we can expect smaller systematic errors due to the uncertainty of the calorimeter scale and detector corrections. Furthermore in the region of higher Q^2 the resolved component of the photon is suppressed, therefore the ambiguity between CASCADE-like and RAPGAP-like descriptions may vanish. Another possibility was considered by Kwieciński et al. [205] who studied deep inelastic events containing a forward photon as a probe of small-x dynamics. The great advantage is that such a measurement is no longer dependent on the hadronization mechanism. At an integrated luminosity of around $1\,{\rm fb}^{-1}$ we can expect about 300 BFKL-like events within the following phase space cuts: $20 < Q^2 < 30, k_{\gamma\perp}^2 > 5\,{\rm GeV}^2, \Theta_\gamma > 5°$, where $k_{\gamma\perp}$ and Θ_γ are the transverse momenta and the angle of the forward photon, respectively.[13] The DGLAP theory prediction is about 3.5 times lower. This process seems to be measurable at HERA 2; however, the background from π^0's may turn out to be large.

4.2.2 Forward π^0 mesons

H1 recently measured single forward π^0 meson production [156]. This new measurement triples the number of π^0's in comparison to previously published data [151], allowing the measurement of more differential distributions and additional final-state observables. The analysis is restricted to the kinematic range $2 < Q^2 < 70\,{\rm GeV}^2$, $5° < \theta_\pi < 25°$, $x_\pi = E_\pi/E_p > 0.01$ (lab. system) and $p_{\rm T,\pi}^\star > 2.5\,{\rm GeV}$ (hcms). The differential cross section as a function of Bjorken variable x for different regions in Q^2 is shown in Fig. 31. It should be noted that this measurement covers a range in x down to $4 \cdot 10^{-5}$. The prediction of a DGLAP based Monte Carlo (RAPGAP DIR) is well below the data, whereas a reasonable description is obtained when the resolved virtual photon contribution is added (RAPGAP RES). It should be also noted, that a rather

---

[13] It is necessary to impose an isolation cut on the photon to suppress background from π^0's produced within outgoing quark jet. Experimentally one requires that within the isolation cone around the photon the energy deposit is below a few percent of the photon energy.
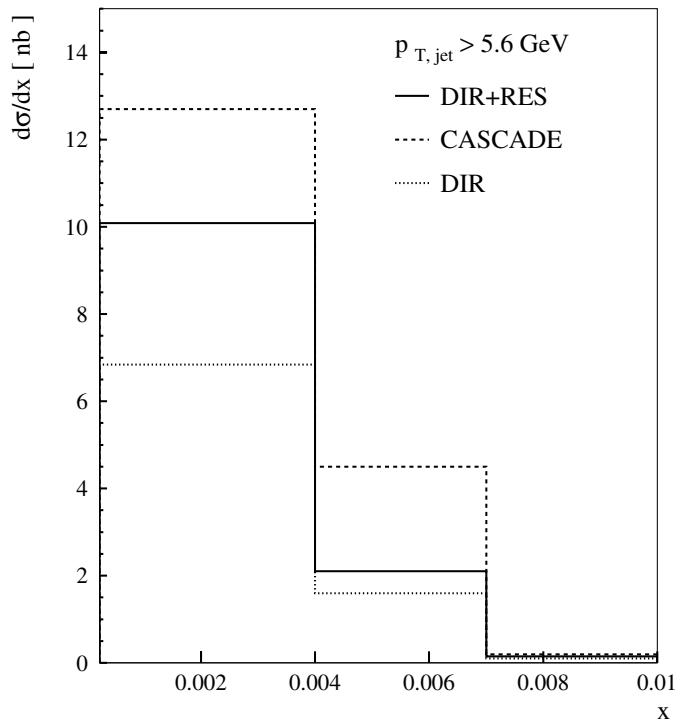

Fig. 30. Forward jet cross section as a function of the Bjorken variable x in the new cut scenario designed for high statistics data: $Q^2 > 16\,{\rm GeV}^2, p_{\rm T,jet} > 5\,{\rm GeV}, x_{\rm jet} > 0.05, 0.1 < y < 0.7$
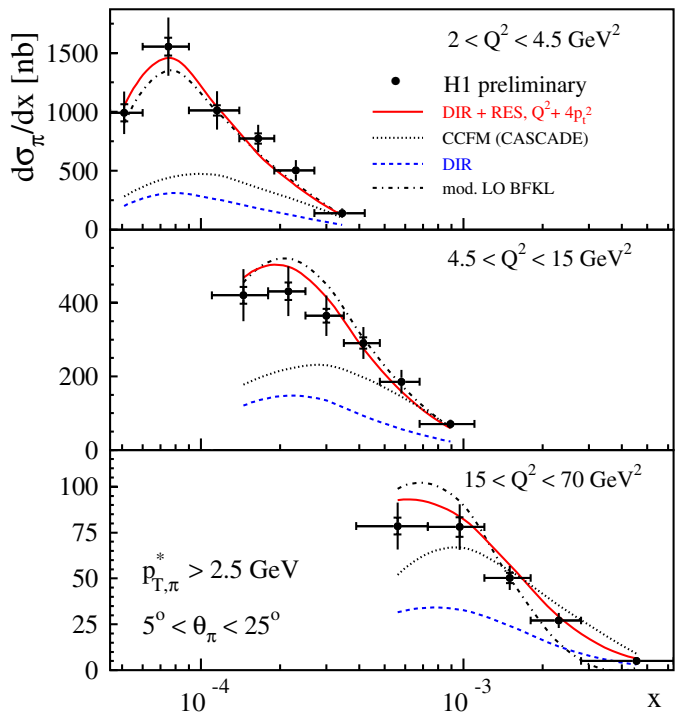

Fig. 31. The cross section for forward π^0 production as a function of x for $p_{\rm T,\pi^0}^\star > 2.5\,{\rm GeV}$. Also shown are the predictions from various Monte Carlo calculations

large factorization and renormalization scale $Q^2 + 4p_\perp{}^2$ has to be used in this case. Surprisingly, CASCADE (all sets, but only JS2001 is shown) falls below the data at small x

values. The fact that CASCADE, which provides good description of the forward jet production, fails to describe the forward π^0 production at small x is interesting in itself. It may indicate that quark initiated cascades and final-state cascades (gluon splitting into quark pairs), both missing in present CASCADE generator code, play an important role in the forward π^0 production. In RAPGAP both processes contribute significantly to the forward π^0 cross section, influencing both the scale for string fragmentation (string invariant mass) and the string composition (quark versus gluon fragmentation). The final effect is such that RAPGAP is able to produce significantly more forward π^0's. It is interesting to note that the parton to hadron fragmentation usually viewed as a complication of the partonic picture of deep inelastic collisions, here may serve also as the indicator of the underlying parton dynamics.

It should be stressed, however, that there is no direct contradiction in the data: discrepancies in the π^0 cross section arise in the region of x which is mostly beyond the reach of the forward jet measurement. It is interesting to note that the previously mentioned BFKL calculation of the forward jet cross section [204] is consistent with the forward π^0 mesons measurement (dashed-dotted curve). The BFKL prediction for the π^0 cross section was obtained by the convolution of the parton distribution of KMO [204] with the KKP (Kniehl, Kramer, Pötter) fragmentation function [206].

We expect that different initial-state cascade dynamics should lead to different radiation patterns and therefore to a different transverse energy flow. The transverse energy flow in the hadronic center of mass system, $\frac{1}{N}dE_T^\star/d(\eta^\star - \eta_\pi^\star)$, in events containing at least one forward π^0 is presented in Fig. 32, where $\eta_\pi^\star$ gives the pseudorapidity of the pion (in the hcms). The spectra are presented in three intervals of the π^0 pseudorapidity: $-1.25 < \eta_\pi^\star < -0.25$ (closest to proton direction), $-0.25 < \eta_\pi^\star < 0.25$ and $0.25 < \eta_\pi^\star < 2.0$ (farthest from proton direction).

The QCD based approaches all describe the transverse energy flow around the π^0 but give different predictions in the *current* region. The resolved photon picture gives a reasonable description of the spectra whilst the CCFM approach overestimates the transverse energy flow when the forward π^0 is closest to the proton direction (top left). The direct photon model gives the worst description of the data. It predicts a transverse energy flow which rises strongly with increasing $\Delta\eta^\star$ and shows a peak at large values of pseudorapidity difference. This effect becomes less pronounced with increasing pseudorapidity of the forward π^0. The differences between the models can be qualitatively understood as a consequence of the ordering criteria of the parton cascade implemented in various Monte Carlo generators.

4.2.3 Dijet production at the Tevatron

The jet production data at high-energy hadron–hadron colliders can also be used to test parton evolution dynamics. The production of exactly two jets is described at LO by

an α_s^2 calculation as being back-to-back in azimuthal angle and having their transverse momenta balanced. Higher order processes involve the radiation of additional partons, which will upset this correlation, and additional soft radiation in higher order processes will decrease the correlation further, leading to a smearing of the $\Delta\phi$ distribution. Perturbative QCD has been successful in describing dijet production up to next-to-leading order, whereas higher order contributions have to be accounted for by parton shower models. Since the production mechanism may involve more than one hard interaction scale, a different treatment of the parton radiation, such as BFKL, might be needed.

The D0 experiment has studied events in which two jets, widely separated in rapidity, have been identified. Due to their uniform calorimetric coverage of ± 4 units in rapidity this experiment is well suited for such an investigation. Jets were defined using a cone algorithm and $E_{t\,jet} > 20$ GeV. In a multi-jet event the two jets mostly separated were chosen for the analyses provided one of them had $E_t > 50$ GeV; this in order to avoid any trigger inefficiency.

If $\langle\cos(\pi - \Delta\phi)\rangle$ is plotted as a function of the rapidity separation between the observed jets, then one would expect to observe a decrease in this variable as the rapidity separation increases, simply because the phase space for additional radiation increases. As shown in Fig. 33 the D0 experiment [207] also observes a linear decrease with the pseudorapidity interval, well described by the HERWIG Monte Carlo. The JETRAD Monte Carlo, which provides a NLO dijet calculation, predicts less de-correlation at large rapidity gaps. The BFKL calculation by [70], valid for large s, on the other hand gives much larger de-correlation ef-
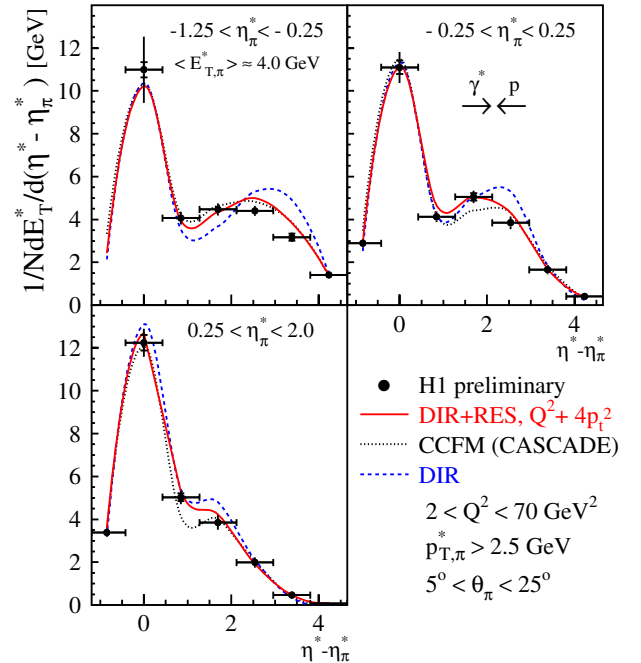

Fig. 32. The distribution of the transverse energy as a function of the pseudorapidity difference in different intervals of the π^0 pseudorapidity. Predictions of three QCD based models are shown
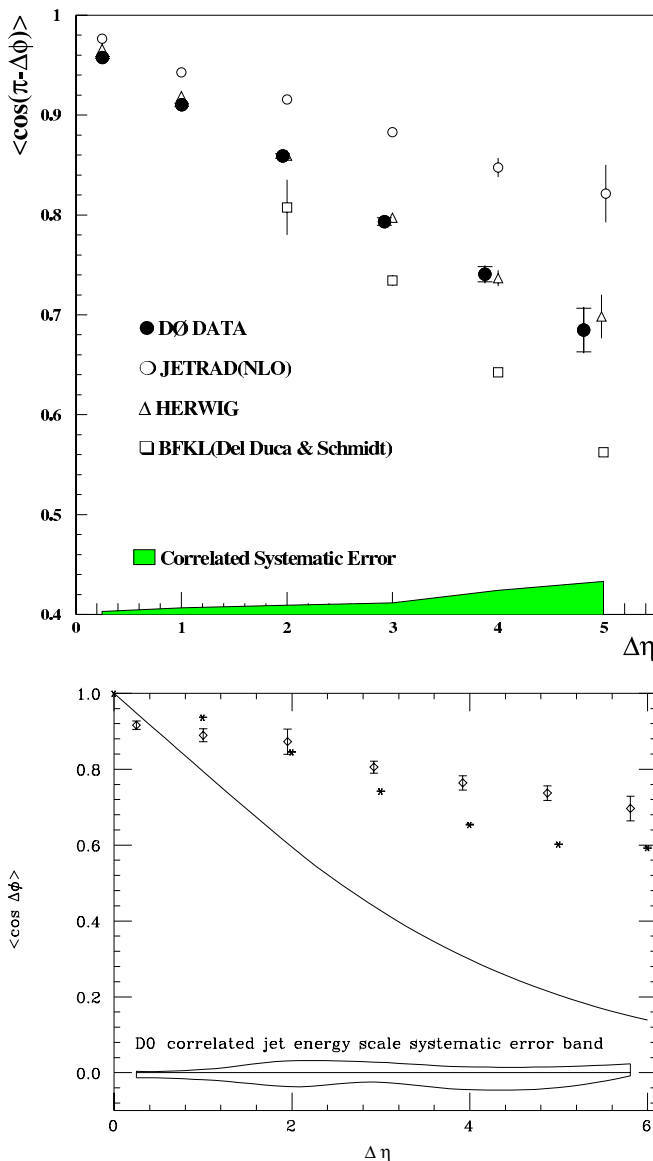
Fig. 33. The average dijet azimuthal correlation $cos(\pi - \Delta\phi)$ as a function of $\Delta\eta$. **a** Comparison with NLO, HERWIG and a BFKL calculation [70] taken from [207]. **b** Comparison with the BFKL calculation satisfying energy/momentum conservation [55]

the data. Especially the implemented cut on the maximum allowed transverse momentum of jets invalidates a BFKL analysis based on the asymptotic behavior of the BFKL prediction. Such a cut will of course always be implicitly implemented by the constraint in energy at a given collider, necessitating a detailed analysis as described in Sect. 3.3. (2) As the cuts on the transverse momenta of trigger jets were chosen equal, the fixed NLO QCD calculations of both the total dijet rates and the azimuthal de-correlations are plagued with large logarithms of perturbative, non-BFKL origin.

The constrained phase space at the Tevatron for dijets with large rapidity separation puts severe limits on the phase space for mini-jets (contributing to the BFKL evolution). The phase space constraint prohibits the rise in cross section with increasing rapidity separation (simply because the decrease in the PDFs is faster than the increase in the partonic cross section), but other observables, like the angular correlation of dijets, still get large BFKL corrections. The LHC promises to be very well suited for a study of effects from the BFKL evolution.

4.3 Experimental conclusions and outlook

The measurements of forward jets and particles are sensitive to the dynamics of parton evolution. Several QCD based approaches have been confronted with the data. It has been shown that NLO dijet DGLAP calculations fall well below forward jet data. The forward jet cross section is, however, well described by a DGLAP based Monte Carlo which includes a resolved photon component. Similarly, results obtained using the BFKL and CCFM evolution schemes are compatible with the data. The measurement of the forward π^0 cross section leads essentially to the same conclusions for the region of Bjorken variable x covered by the forward jet measurements. For the lowest values of x i.e. those beyond the reach of the forward jet measurements, the CASCADE Monte Carlo generator fails to describe the data, possibly due to missing quark initiated cascades. The comparison of results from various models seems to indicate some sensitivity to the fragmentation method used to connect the parton and hadron levels. Study of the transverse energy flow associated with forward π^0's seems to favor the DGLAP direct + resolved approach.

However, the present measurements at HERA were mainly restricted by two factors: the available center of mass energy and the geometrical acceptance of the detectors, requiring the forward jet to lie between: $2 \overset{<}{\sim} \eta \overset{<}{\sim} 3$. The dijet measurements are described best with a different scale (RAPGAP) or unintegrated gluon density (CASCADE) than the forward jet measurements (cf. Table 2). This shows that indeed new effects are seen: if the forward jet cross section is extended to a range of η_{jet} up to 6 units (as proposed in the proposals for a continued HERA3 program [208, 209]) the difference compared to DGLAP becomes even more significant.

fects, although we note that in this analysis, large effects from the constraint of energy and momentum conservation have been ignored in the BFKL evolution. In fact, if these are taken into account as describe in Sect. 3.3 the BFKL prediction is in much better agreement with the data [55].

Recently the D0 measurements of Mueller–Navelet jets at the Tevatron have been discussed in detail by Andersen et al. [59], therefore we restrict ourselves to quoting their main conclusions.
(1) Definitions of the momentum fractions used by D0 and some of the acceptance cuts imposed spoil the correctness of the procedure to extract the effective BFKL intercept from

5 Conclusions

On the theoretical side, significant progress in understanding small-x effects has been made. The soft region ($k_\perp \stackrel{<}{\sim} 1\,\mathrm{GeV}$) has been clearly identified to have a significant influence on the hadronic final-state observables. With the consistent treatment of the scale in α_s and including the non-singular terms into the CCFM splitting function, a necessary step forward to a serious application of the CCFM small-x evolution equation has been taken.

The question of gauge invariance of the whole $k_\perp$-factorization approach in general and also the question of gauge invariance of (integrated or unintegrated) PDFs has been clarified further.

Many new measurements in the area of small-x physics have been made public, and the interest in a better understanding of small-x effects is very clear. New measurements indicate the need to go even beyond $\mathcal{O}(\alpha_s^3)$ if calculations are performed in the collinear factorization approach. On the other hand, these effects are automatically included in $k_\perp$-factorization, which makes $k_\perp$-factorization an important tool for studying higher order corrections. It was shown that, irrespective of the particular choice of the non-perturbative CO matrix elements, the production of J/ψ mesons at HERA can be reasonably well described within the color-singlet production mechanism (within $k_\perp$-factorization) and color octet contributions are not at all needed. More accurate measurements of the polarization properties of the J/ψ mesons will be an interesting test of the $k_\perp$-factorization predictions.

Still, results from the experiments at HERA and the Tevatron have not yet provided unambiguous evidence for new small-x effects. Including higher orders in the calculation according to the collinear approach and/or including the concept resolved (virtual) photons seems to mimic also new small-x effects. In order to unambiguously identify small-x effects at e.g. HERA, it is necessary to increase the angular coverage of the experimental setup towards the proton direction, as has been shown in the proposal for an extended HERA running beyond 2006, the so-called HERA 3 scenario. Since a correct description of the small-x dynamics is essential for the understanding of QCD at high energies, and also for any asymptotically free field theory it is of great importance to continue and extend the experimental and theoretical efforts.

References

1. Small x Collaboration, B. Andersson et al., Eur. Phys. J. C **25**, 77 (2002), hep-ph/0204115
2. B. Andersson, G. Gustafson, J. Samuelsson, Nucl. Phys. B **467**, 443 (1996)
3. B. Andersson, G. Gustafson, H. Kharraziha, J. Samuelsson, Z. Phys. C **71**, 613 (1996)
4. G. Gustafson, H. Kharraziha, L. Lönnblad, The LCD Event Generator, in Proceedings of the Workshop on Future Physics at HERA, edited by A. De Roeck, G. Ingelman, R. Klanner (1996), p. 620
5. H. Kharraziha, L. Lönnblad, JHEP **03**, 006 (1998)
6. H. Jung, G. Salam, Eur. Phys. J. C **19**, 351 (2001), hep-ph/0012143
7. H. Jung, Comp. Phys. Comm. **143**, 100 (2002), http://www.quark.lu.se/ hannes/cascade/+
8. V. Gribov, L. Lipatov, Sov. J. Nucl. Phys. **15**, 438, 675 (1972)
9. L. Lipatov, Sov. J. Nucl. Phys. **20**, 94 (1975)
10. G. Altarelli, G. Parisi, Nucl. Phys. B **126**, 298 (1977)
11. Y. Dokshitser, Sov. Phys. JETP **46**, 641 (1977)
12. E. Kuraev, L. Lipatov, V. Fadin, Sov. Phys. JETP **44**, 443 (1976)
13. E. Kuraev, L. Lipatov, V. Fadin, Sov. Phys. JETP **45**, 199 (1977)
14. Y. Balitskii, L. Lipatov, Sov. J. Nucl. Phys. **28**, 822 (1978)
15. M. Ciafaloni, Nucl. Phys. B **296**, 49 (1988)
16. S. Catani, F. Fiorani, G. Marchesini, Phys. Lett. B **234**, 339 (1990)
17. S. Catani, F. Fiorani, G. Marchesini, Nucl. Phys. B **336**, 18 (1990)
18. G. Marchesini, Nucl. Phys. B **445**, 49 (1995)
19. J.R. Forshaw, A. Sabio Vera, Phys. Lett. B **440**, 141 (1998)
20. B.R. Webber, Phys. Lett. B **444**, 81 (1998)
21. G. Salam, JHEP **03**, 009 (1999)
22. J. Kwiecinski, A.D. Martin, A.M. Staśto, Phys. Rev. D **56**, 3991 (1997)
23. M.A. Kimber, A.D. Martin, M.G. Ryskin, Phys. Rev. D **63**, 114027 (2001)
24. J.C. Collins, Acta Phys. Polon. B **34**, 3103 (2003)
25. Y.L. Dokshitzer, D. Diakonov, S.I. Troian, Phys. Rept. **58**, 269 (1980)
26. J.C. Collins, D.E. Soper, Nucl. Phys. B **194**, 445 (1982)
27. J.C. Collins, D.E. Soper, Nucl. Phys. B **193**, 381 (1981); Erratum B **213**, 545 (1981)
28. L. Gribov, E. Levin, M. Ryskin, Phys. Rep. **100**, 1 (1983)
29. E.M. Levin, M.G. Ryskin, Y.M. Shabelski, A.G. Shuvaev, Sov. J. Nucl. Phys. **53**, 657 (1991)
30. S. Catani, M. Ciafaloni, F. Hautmann, Nucl. Phys. B **366**, 135 (1991)
31. J. Collins, R. Ellis, Nucl. Phys. B **360**, 3 (1991)
32. M. Ademollo, A. Bellini, M. Ciafaloni, Phys. Lett. B **223**, 318 (1989)
33. M. Ciafaloni, G. Camici, Phys. Lett. B **430**, 349 (1998)
34. M. Ciafaloni, D. Colferai, Phys. Lett. B **452**, 372 (1999)
35. J. Bartels, D. Colferai, G.P. Vacca, Eur. Phys. J. C **24**, 83 (2002)
36. J. Bartels, D. Colferai, S. Gieseke, A. Kyrieleis, Phys. Rev. D **66**, 094017 (2002)
37. J. Bartels, D. Colferai, G.P. Vacca, Eur. Phys. J. C **29**, 235 (2003)
38. J. Bartels, D. Colferai, G.P. Vacca, The NLO jet vertex for Mueller–Navelet and forward jets: The quark part, 2001, hep-ph/0112283, to be published in Phys. Rev. D
39. J. Bartels, S. Gieseke, A. Kyrieleis, in preparation
40. H. Jung, Acta Phys. Polon. B **33**, 2995 (2002)

41. M. Hansson, H. Jung, The status of CCFM unintegrated gluon densities, in DIS 2003, XI International Workshop on Deep Inelastic Scattering, St. Petersburg, Russia (2003), hep-ph/0309009

42. H1 Collaboration, S. Aid et al., Nucl. Phys. B **470**, 3 (1996)

43. H1 Collaboration, C. Adloff et al., Eur. Phys. J. C **21**, 33 (2001)

44. ZEUS Collaboration, M. Derrick et al., Z. Phys. C **72**, 399 (1996)

45. ZEUS Collaboration, S. Chekanov et al., Eur. Phys. J. C **21**, 443 (2001)

46. B.R. Webber, Nucl. Phys. C Proc. Suppl. C **18**, 38 (1990)

47. G. Marchesini, B. Webber, Nucl. Phys. B **349**, 617 (1991)

48. G. Marchesini, B. Webber, Nucl. Phys. B **386**, 215 (1992)

49. J. Kwiecinski, A. Martin, P. Sutton, Z. Phys. C **71**, 585 (1996)

50. J. Kwieciński, Acta. Phys. Polon B **33**, 1809 (2002)

51. A. Gawron, J. Kwiecinski, Acta Phys. Polon. B **34**, 133 (2003)

52. M.A. Kimber, A.D. Martin, M.G. Ryskin, Eur. Phys. J. C **12**, 655 (2000)

53. A.H. Mueller, H. Navelet, Nucl. Phys. B **282**, 727 (1987)

54. V.S. Fadin, L.N. Lipatov, Phys. Lett. B **429**, 127 (1998)

55. L.H. Orr, W.J. Stirling, Phys. Rev. D **56**, 5875 (1997)

56. C.R. Schmidt, Phys. Rev. Lett. **78**, 4531 (1997)

57. J.R. Andersen, W.J. Stirling, JHEP **02**, 018 (2003)

58. L.H. Orr, W.J. Stirling, Phys. Lett. B **429**, 135 (1998)

59. J.R. Andersen et al., JHEP **02**, 007 (2001)

60. J.R. Andersen, V.D. Duca, F. Maltoni, W.J. Stirling, JHEP **05**, 048 (2001)

61. J.R. Andersen, A. Sabio Vera, Phys. Lett. B **567**, 116 (2003)

62. J.R. Andersen, A. Sabio Vera, The gluon Green's function in the BFKL approach at next-to-leading logarithmic accuracy (2003), hep-ph/0309331

63. M. Ciafaloni, D. Colferai, G.P. Salam, A.M. Stasto, Phys. Rev. D **68**, 114003 (2003)

64. M. Ciafaloni et al., Phys. Lett. B **576**, 143 (2003)

65. G. Altarelli, R.D. Ball, S. Forte, Nucl. Phys. B **674**, 459 (2003)

66. R.S. Thorne, Phys. Rev. D **64**, 074005 (2001)

67. R.S. Thorne, Phys. Rev. D **60**, 054031 (1999)

68. W.J. Stirling, Nucl. Phys. B **423**, 56 (1994)

69. V. Del Duca, C.R. Schmidt, Phys. Rev. D **49**, 4510 (1994)

70. V. Del Duca, C.R. Schmidt, Phys. Rev. D **51**, 2150 (1995)

71. I. Balitsky, Nucl. Phys. B **463**, 99 (1996)

72. Y.V. Kovchegov, Phys. Rev. D **60**, 034008 (1999)

73. M. Braun, Eur. Phys. J. C **16**, 337 (2000)

74. M. Lublinsky, E. Gotsman, E. Levin, U. Maor, Nucl. Phys. A **696**, 851 (2001)

75. K. Golec-Biernat, L. Motyka, A.M. Staśto, Phys. Rev. D **65**, 074037 (2002)

76. K. Golec-Biernat, A.M. Staśto, Nucl. Phys. B **668**, 345 (2003)

77. E. Gotsman, E. Levin, M. Lublinsky, U. Maor, Eur. Phys. J. C **27**, 411 (2003)

78. K. Golec-Biernat, M. Wüsthoff, Phys. Rev. D **59**, 014017 (1998)

79. K. Golec-Biernat, M. Wüsthoff, Phys. Rev. D **60**, 114023 (1999)

80. A.M. Staśto, K. Golec-Biernat, J. Kwiecinski, Phys. Rev. Lett. **86**, 596 (2001)

81. M. Lublinsky, Eur. Phys. J. C **21**, 513 (2001)

82. ZEUS Collaboration, J. Breitweg et al., Phys. Lett. B **487**, 53 (2000)

83. H1 Collaboration, C. Adloff et al., hep-ex/0304003

84. E665 Collaboration, M. Adams et al., Phys. Rev. D **54**, 3006 (1996)

85. E.V. Shuryak, I. Zahed, Understanding the non-perturbative deep-inelastic scattering: Instanton-induced inelastic dipole dipole cross section, hep-ph/0307103

86. H. Kowalski, D. Teaney, An impact parameter dipole saturation model, hep-ph/0304189

87. T. Sjostrand, M. van Zijl, Phys. Rev. D **36**, 2019 (1987)

88. H1 Collaboration, S. Aid et al., Z. Phys. C **70**, 17 (1996)

89. ZEUS Collaboration, J. Breitweg et al., Eur. Phys. J. C **1**, 109 (1998)

90. C. Gwenlan, Acta Phys. Polon. B **33**, 3123 (2002)

91. G. Gustafson, L. Lönnblad, G. Miu, Phys. Rev. D **67**, 034020 (2003)

92. M. Maul, Phys. Rev. D **65**, 094010 (2002), hep-ph/0111031

93. J. Kwiecinski, M. Maul, Phys. Rev. D **67**, 034014 (2003)

94. J. Kwiecinski, B. Ziaja, Phys. Rev. D **60**, 054004 (1999), hep-ph/9902440

95. J. Bartels, B.I. Ermolaev, M.G. Ryskin, Z. Phys. C **70**, 273 (1996); Z. Phys. C **72**, 627 (1996)

96. R. Kirschner, L.N. Lipatov, Nucl. Phys. B **213**, 122 (1983)

97. R. Kirschner, Z. Phys. C **67**, 459 (1995), hep-ph/9404158

98. M. Glück, E. Reya, M. Stratmann, W. Vogelsang, Phys. Rev. D **63**, 094005 (2001), hep-ph/0011215

99. M. Glück, E. Reya, A. Vogt, Eur. Phys. J. C **5**, 461 (1998), hep-ph/9806404

100. E. Braaten, S. Fleming, Phys. Rev. Lett. **74**, 3327 (1995)

101. E. Braaten, T.C. Yuan, Phys. Rev. D **52**, 6627 (1995)

102. P.L. Cho, A.K. Leibovich, Phys. Rev. D **53**, 150 (1996)

103. P.L. Cho, A.K. Leibovich, Phys. Rev. D **53**, 6203 (1996)

104. G.T. Bodwin, E. Braaten, G.P. Lepage, Phys. Rev. D **51**, 1125 (1995)

105. A. Likhoded, talk at Heavy Quark Workshop at Weizmann Institute, Israel, 2003

106. S. Fleming, T. Mehen, Phys. Rev. D **57**, 1846 (1998)

107. B.A. Kniehl, L. Zwirner, Nucl. Phys. B **621**, 337 (2002)

108. J.G. Korner, J. Cleymans, M. Kuroda, G.J. Gounaris, Phys. Lett. B **114**, 195 (1982)

109. J.-P. Guillet, Z. Phys. C **39**, 75 (1988)

110. H. Merabet, J.F. Mathiot, R. Mendez-Galain, Z. Phys. C **62**, 639 (1994)

111. F. Yuan, K.-T. Chao, Phys. Rev. D **63**, 034017 (2001)

112. S.P. Baranov, Phys. Lett. B **428**, 377 (1998)

113. P. Hagler et al., Phys. Rev. D **63**, 077501 (2001)

114. F. Yuan, K.-T. Chao, Phys. Rev. Lett. **87**, 022002 (2001)

115. F. Yuan, K.-T. Chao, Phys. Rev. Lett. **87**, 022002 (2001)

116. P. Hagler et al., Phys. Rev. Lett. **86**, 1446 (2001)

117. S.P. Baranov, Phys. Rev. D **66**, 114003 (2002)

118. A.V. Lipatov, N.P. Zotov, Eur. Phys. J. C **27**, 87 (2003)

119. ZEUS Collaboration, S. Chekanov et al., Eur. Phys. J. C **27**, 173 (2003)

120. J. Blümlein, On the k_t dependent gluon density of the proton, in Proceedings of the Workshop on Deep Inelastic Scattering and QCD, edited by J. Laporte, Y. Sirois (1995), DESY 95-121 and hep-ph/9506403

121. H1 Collaboration, C. Adloff et al., Eur. Phys. J. C **25**, 41 (2002)

122. ZEUS Collaboration, J. Breitweg et al., Eur. Phys. J. C **12**, 35 (1999), DESY 99-101

123. H1 Collaboration, C. Adloff et al., Phys. Lett. B **528**, 199 (2002), hep-ex/0108039
124. S.P. Baranov et al., Eur. Phys. J. C **24**, 425 (2002)
125. ZEUS Collaboration, J. Breitweg et al., Eur. Phys. J. C **6**, 67 (1999)
126. M. Cacciari, S. Frixione, P. Nason, JHEP **0203**, 053 (2002)
127. S. Baranov, N. Zotov, Phys. Lett. B **458**, 389 (1999)
128. S. Baranov, H. Jung, N. Zotov, Charm production in the semi-hard approach of QCD, in Proceedings of the Workshop on Monte Carlo generators for HERA physics, edited by A. Doyle, G. Grindhammer, G. Ingelman, H. Jung (DESY, Hamburg 1999), p. 484, hep-ph/9910210
129. S. Baranov, N. Zotov, Phys. Lett. B **491**, 111 (2000)
130. V. Chiochia, for H1 and ZEUS collaborations, Nucl. Phys. B Proc. Suppl. **117**, 329 (2002)
131. T. Sloan, for the H1 Collaboration, Heavy flavor production at HERA, in 36th Rencontres de Moriond on QCD and Hadronic Interactions, Les Arcs, France (2001), hep-ex/0105064
132. H1 Collaboration, C. Adloff et al., Measurements of beauty production using semi-muonic decays, 2003, contribution to EPS03, July 17–23, Aachen (Abstract 117)
133. ZEUS Collaboration, J. Breitweg et al., Eur. Phys. J. C **18**, 625 (2001)
134. H. Jung, Unintegrated parton densities applied to heavy quark production in the CCFM approach, in Proceedings of the Rinberg workshop on New trends in HERA physics, Ringberg Castle, Tegernsee, Germany, hep-ph/0109146
135. H. Jung, Phys. Rev. D **65**, 034015 (2002), DESY-01-136, hep-ph/0110034
136. H1 Collaboration, C. Adloff et al., Phys. Lett. B **467**, 156 (1999), and erratum ibid
137. ZEUS Collaboration, J. Breitweg et al., Phys. Lett. B **479**, 37 (2000)
138. H1 Collaboration, T. Ahmed et al., Eur. Phys. J. C **13**, 415 (2000), DESY 98-076 and hep-ex/9806029
139. H1 Collaboration, A. Aktas et al., Inclusive dijet production at low Bjorken-x in deep inelastic scattering, 2003, DESY-03-160, hep-ex/0310019
140. ZEUS Collaboration, J. Breitweg et al., Eur. Phys. J. C **11**, 35 (1999), DESY 99-057
141. H1 Collaboration, C. Adloff et al., Eur. Phys. J. C (2003)
142. H1 Collaboration, C. Adloff et al., Phys. Lett. B **483**, 36 (2000)
143. H1 Collaboration, I. Abt et al., Z. Phys. C **63**, 377 (1994), DESY 94-033
144. H1 Collaboration, C. Adloff et al., Nucl. Phys. B **485**, 3 (1997)
145. H. Jung, L. Jonsson, H. Kuster, unpublished, hep-ph/9805396
146. H1 Collaboration, S. Aid et al., Phys. Lett. B **356**, 118 (1995)
147. H1 Collaboration, C. Adloff et al., Eur. Phys. J. C **12**, 595 (2000)
148. H1 Collaboration, C. Adloff et al., Nucl. Phys. B **538**, 3 (1999)
149. H. Jung, for H1 and ZEUS collaborations, Nucl. Phys. B Proc. Suppl. **117**, 352 (2002)
150. ZEUS Collaboration, J. Breitweg et al., Eur. Phys. J. C **6**, 239 (1999)
151. H1 Collaboration, C. Adloff et al., Nucl. Phys. B **538**, 3 (1999)
152. ZEUS Collaboration, J. Breitweg et al., Phys. Lett. B **474**, 223 (2000)
153. G. Kramer, B. Potter, Phys. Lett. B **453**, 295 (1999)
154. H. Jung, L. Jonsson, H. Kuster, Eur. Phys. J. C **9**, 383 (1999), hep-ph/9903306
155. H1 Collaboration, C. Adloff et al., Phys. Lett. B **462**, 440 (1999)
156. L. Goerlich, for H1 collaboration, Acta Phys. Polon. B **33**, 3287 (2002)
157. S.P. Baranov, N.P. Zotov, J. Phys. G **29**, 1395 (2003)
158. H1 Collaboration, T. Ahmed et al., Phys. Lett. B **338**, 507 (1994)
159. M. Krämer, Nucl. Phys. B **459**, 3 (1996)
160. M. Krämer, Prog. Part. Nucl. Phys. **47**, 141 (2001)
161. V.A. Saleev, N.P. Zotov, Mod. Phys. Lett A **9**, 151 (1994); Erratum A **9**, 1517 (1994)
162. V.A. Lipatov, V.A. Saleev, N.P. Zotov, Mod. Phys. Lett A **15**, 695 (2000)
163. S.P. Baranov, Phys. Lett. B **428**, 377 (1998)
164. A.V. Lipatov, L. Lönnblad, N.P. Zotov, JHEP **0401**, 010 (2004)
165. H. Jung, Mod. Phys. Lett. A **19**, 1 (2004), hep-ph/0311249
166. M.A. Sanchis-Lozano, B. Cano-Coloma, Phys. Lett. B **406**, 232 (1997)
167. M.A. Sanchis-Lozano, B. Cano-Coloma, Nucl. Phys. B **508**, 753 (1997)
168. E. Braaten, M. Beneke, J. Lee, Phys. Rev. D **62**, 094005 (2000)
169. R.D. Field, Phys. Rev. D 65 (2002) 094006
170. S. Frixione, M. Mangano, P. Nason, G. Ridolfi, Nucl. Phys. B **431**, 453 (1994)
171. P. Hagler et al., Phys. Rev. D **62**, 071502 (2000)
172. N.P. Zotov, V.A. Lipatov, V.A. Saleev, Phys. At. Nucl. **66**, 755 (2003)
173. S.P. Baranov, V.A. Lipatov, N.P. Zotov, hep-ph/0302171 (2003)
174. G. Ingelman, A. Edin, J. Rathsman, Comp. Phys. Comm. **101**, 108 (1997)
175. H. Jung, The RAPGAP Monte Carlo for Deep Inelastic Scattering, version 2.08, Lund University, 2002, http://www.quark.lu.se/ hannes/rapgap/+
176. ZEUS Collaboration, S. Chekanov et al., Phys. Rev. D **67**, 012007 (2003)
177. A. Mueller, Nucl. Phys. B Proc. Suppl. C **18**, 125 (1990)
178. A. Mueller, J. Phys. G **17**, 1443 (1991)
179. J. Bartels et al., Phys. Lett. B **384**, 300 (1996), hep-ph/9604272
180. B. Potter, Comput. Phys. Commun. **133**, 105 (2000)
181. G. Kramer, B. Potter, Eur. Phys. J. C **5**, 665 (1998)
182. B. Potter, J. Phys. G **28**, 871 (2002)
183. S. Catani, M.H. Seymour, Nucl. Phys. B **485**, 291 (1997)
184. J. Pumplin et al., JHEP **07**, 012 (2002)
185. J.C. Collins, X.-M. Zu, JHEP **06**, 018 (2002)
186. ZEUS Collaboration, S. Chekanov et al., Phys. Rev. D **67**, 012007 (2003)
187. E.M. Lobodzinska, DIS 2003, St. Petersburg, hep-ph/0311180
188. B. Badelek, J. Kwiecinski, A. Staśto, Z. Phys. C **74**, 297 (1997)
189. A.D. Martin, R.G. Roberts, W.J. Stirling, R.S. Thorne, Phys. Lett. B **531**, 216 (2002)
190. H1 Collaboration, C. Adloff et al., Eur. Phys. J. C **19**, 289 (2001)

191. ZEUS Collaboration, J. Breitweg et al., Phys. Lett. B **507**, 70 (2001)

192. D0 Collaboration, B. Abbott et al., Phys. Rev. Lett. **82**, 2457 (1999)

193. H1 Collaboration, C. Adloff et al., Phys. Lett. B **542**, 193 (2002)

194. S. Catani, Y. Dokshitzer, B. Webber, Phys. Lett. B **285**, 291 (1992)

195. S. Catani, Y. Dokshitzer, M. Seymour, B. Webber, Nucl. Phys. B **406**, 187 (1993)

196. G. Schuler, T. Sjöstrand, Phys. Lett. B **376**, 193 (1996)

197. ZEUS Collaboration, J. Breitweg et al., Inclusive jet production in neutral current deep inelastic scattering at HERA and parton dynamics at low x, 2003, contribution to EPS03, July 17–23, Aachen (Abstract 507)

198. M. Klasen, G. Kramer, Phys. Lett. B **366**, 385 (1996)

199. S. Frixione, G. Ridolfi, Nucl. Phys. B **507**, 315 (1997)

200. A.J. Askew, D. Graudenz, J. Kwiecinski, A.D. Martin, Phys. Lett. B **338**, 92 (1994)

201. J.R. Forshaw, R.G. Roberts, Phys. Lett. B **335**, 494 (1994)

202. J. Kwiecinski, A.D. Martin, A.M. Staśto, Phys. Lett. B **459**, 644 (1999)

203. A. Szczurek, N.N. Nikolaev, W. Schafer, J. Speth, Phys. Lett. B **500**, 254 (2001)

204. J. Kwiecinski, A.D. Martin, J.J. Outhwaite, Eur. Phys. J. C **9**, 611 (1999), hep-ph/9903439

205. J. Kwiecinski, S.C. Lang, A.D. Martin, Phys. Rev. D **54**, 1874 (1996)

206. B.A. Kniehl, G. Kramer, B. Potter, Nucl. Phys. B **597**, 337 (2001)

207. D0 Collaboration, S. Abachi et al., Phys. Rev. Lett. **77**, 595 (1996)

208. H. Abramowicz et al., A new experiment for the HERA collider. Expression of Interest, MPP-2003-62

209. T. Alexopoulos et al., Electron deuteron scattering with HERA, a letter of Intend for and Experimental Programme with the H1 detector, 2003, http://www-h1.desy.de/h1/www/publications/H1eDLoI.pdf+